Experimental and modeling study of thermoelectric materials for high

figure of merit

Long Chen

A Dissertation presented to the Graduate Faculty

of the University of Virginia in Candidacy for the Degree of

Doctor of Philosophy

Department of Physics

University of Virginia

January 2017

Abstract

Half-Heusler alloys RNiSn (R=Hf, Zr, Ti) were made by arc melting under argon atmosphere followed by the consolidation using Spark Plasma Sintering (SPS) technique. The thermoelectric properties were measured from room temperature up to 1170 K. The temperature dependences of thermoelectric properties and structures were investigated. A frequency-dependent differential effective medium (DEM) model was developed to evaluate the lattice thermal conductivity. This model was also applied to calculate the thermal conductivity of nanostructured Si and $Si_{80}Ge_{20}$ systems. The calculation results were compared with the experimental data measured with time-domain thermoreflectance to investigate length scale effects on phonon wavelength, mean free path, as well as the resulting impact on the thermal conductivity.

In the case of n-type $Hf_{0.6}Zr_{0.4}NiSb_{0.995}Sb_{0.005}$, thermoelectric properties of this composition were conducted by annealing this material near the melting point in order to improve the structural order. The reduction in the lattice strain was observed. It also led to a significant enhancement of the power factor, and thus, the figure of merit (ZT) was raised to 1.2 around 850 K without the need of nanostructures. This large increase in power factor was related to the decrease of carrier concentration and the increase of mobility. This approach can be applied to the broader class of Heusler alloys, and may lead to the improvement of their thermoelectric properties. The elemental substitution and embedment of nanoparticles in the half-Heusler matrix techniques were also investigated to achieve higher ZT. Thermoelectric properties of the substitution of Ti for (Hf, Zr) sites and the addition of nano-ZrO_2 in n-type (Hf, Zr)NiSn were measured. The thermal conductivity of the composition was significantly reduced due to the enhanced phonon

scattering by Ti substitution and the embedded nanoparticles. ZrO_2 also served as potential barriers to scatter carrier that helped enhance the thermopower. A maximum ZT of 1.3 was obtained for $Hf_{0.6}Zr_{0.25}Ti_{0.15}NiSb_{0.995}Sb_{0.005}$ with 2% ZrO_2. In addition, a model accounting for the temperatures dependences of the thermoelectric parameters of both n-type and p-type materials was derived. This model was applied to a unicouple, and gave good agreement with the experimental data. Further, a systematic study was conducted to investigate the role of vanadium (V), niobium (Nb), and tantalum (Ta) as prospective resonant dopants to improve the figure of merit of n-type alloys based on $Hf_{0.6}Zr_{0.4}NiSb_{0.995}Sb_{0.005}$. It was found that the addition of small amounts of V raised the thermopower for the entire temperature range 300-1000 K. In contrast, both Nb and Ta worked as normal dopants, as evident by the decrease in both electrical resistivity and Seebeck coefficient. The variation of thermopower was discussed in terms of carrier scattering mechanisms. The maximum ZT of 1.3 was obtained in $(Hf_{0.6}Zr_{0.4})_{0.99}V_{0.01}NiSb_{0.995}Sb_{0.005}$ alloys. Both the high resistivity and thermopower due to the presence of V introduced resonant states coupled with the reduction in thermal conductivity were responsible for the high figure of merit.

At the end, to evaluate the lattice thermal conductivity, a non-gray differential effective medium (DEM) model was developed and applied to half-Heusler systems. This model not only expanded the applicability of effective medium approach from small volume fractions to the whole range of volume fraction from 0 to 1, but also accounted for the multiple scattering. Then this frequency-dependent effective medium approach was utilized to calculate the lattice thermal conductivity of nanostructured Si and $Si_{80}Ge_{20}$ systems. The model accurately predicted a large reduction in the thermal conductivity of these systems measured with time-domain

thermoreflectance (TDTR). Then the phonon spectral analysis was conducted to investigate length scale effects, and the insight into the role of long wavelength phonons on the thermal conductivity of the nanograined Si and Si-Ge alloys was gained. It was shown that phonons with wavelength much greater than the averaged grain size would not be impacted by the grain boundary scattering.

Table of contents

1. Background of Thermoelectricity.

Thermoelectricity is the direct conversion of temperature difference to electric voltage and vice versa. When there is a temperature difference across the material, an electric voltage is produced or, vice versa, an electric potential difference applied on the material generates a temperature difference. We name the materials capable of doing the heat-electricity energy conversion thermoelectric materials. Thermoelectric materials can be used as refrigerators (thermoelectric coolers) or thermoelectric generators depending on whether converting electricity to heat or the reverse.

1-1. Motivation

In modern world, the demand for energy has grown fast. The conflict between this demand and the limited amount of non-renewable fuels, such as coal, natural gas and oil, is even more severe over the years. On the other hand, the combustion of the fossil fuels has a high impact on the global climate change. The global warming is alarming in recent years, thus it is important to find an alternative and renewable energy. One solution is to generate electricity by converting the waste heat by thermoelectric generators. It is surprising to see that a large amount of heat is wasted in the daily life. For example, the automobiles only take 25% out of the fuel energy as useful portion, as shown in Figure 1-1. The rest of 75% energy is wasted either on exhaust gas or

heating up coolant. Thus, thermoelectric materials can be used to convert the wasted heat into electricity that can support the engine or batteries.
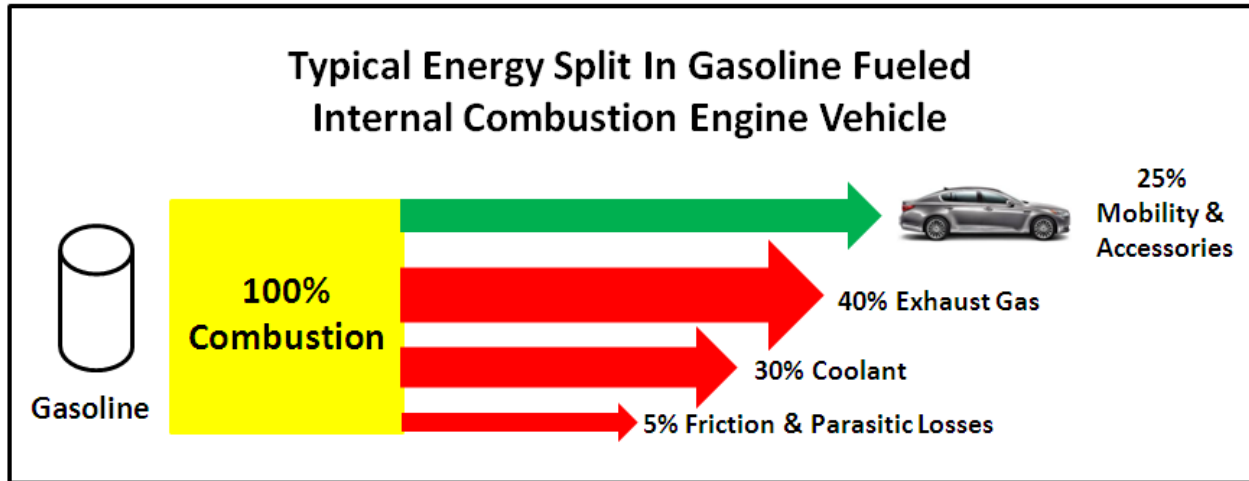
Figure 1-1. A typical energy path for modern gasoline road cars.

So far, the relative low conversion efficiency limits the use the thermoelectric materials. The traditional refrigerators can operate 30% to 90% of the Carnot efficiency, while the most thermoelectric devices have around 10% of the Carnot efficiency. Since there is no known limit for thermoelectric conversion, further research in the field is needed.[1]

1-2. Discovery of Thermoelectric Effects

In 1821, Baltic German physicist Thomas Johann Seebeck discovered that when there was a temperature difference between dissimilar conductors by heating the junctions, a potential

difference was observed. Today, we envisage an open circuit when speaking of the Seebeck effect, as shown in Figure 1-2. The thermoelectric voltage developed by this couple is:

$$\Delta V = V_b - V_a \quad (1\text{-}1)$$

The thermoelectric power of the couple is defined as:

$$S_{AB} = \lim_{\Delta T \to 0} (\Delta V / \Delta T) = \int_{T_a}^{T_b} (S_b - S_a) dT \quad (1\text{-}2)$$

Where ΔV is the electric potential difference across the junction, and S is the magnitude of the thermoelectric voltage in response to the temperature difference.[2]
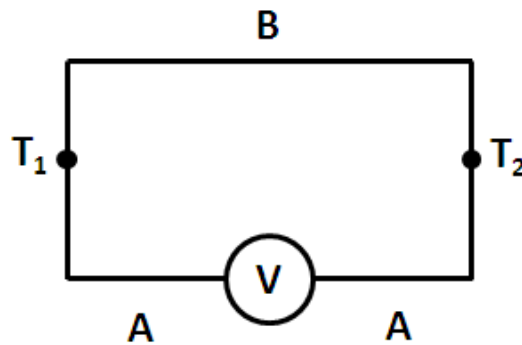
Figure 1-2. An open circuit that displays the Seebeck effect.

In 1834, the second thermoelectric effect was discovered by Jean Charles Athanase Peltier. When a current was made to pass through a junction between two conductors, heat was generated or absorbed based on the direction the flowing current. This heat can be distinguished experimentally from the Joule heat easily since the Joule heat is independent of the direction of current flow. This means the Joule heat is always generated no matter what the direction of the

current flow. On the other hand, the Peltier heat depends linearly in magnitude on the current flow. It can be generated or absorbed. The Peltier effect is shown in Figure 1-3.
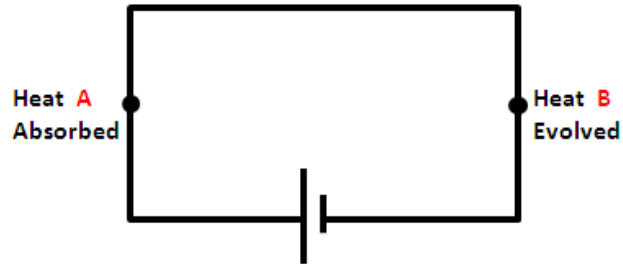
Figure 1-3. The Peltier effect.

According, we can define the Peltier heat generated at the junction per unit time as:

$$\dot{Q} = \Pi_{ab}I = (\Pi_b - \Pi_a)I \quad (1\text{-}3)$$

Where Π_a and Π_b are the Peltier coefficient of conductor a and b, and I is the electric current flowing from a to b.

After analyzing the Seebeck and the Peltier effect, William Thomson in 1854 realized that there should be a thermodynamical connection between the Seebeck potential and the Peltier heat. This led him to postulate the existence of a third thermoelectric effect, which is now called the Thomson heat effect. It can be understood as the following: If an electric current is passing through a homogeneous conductor in the direction of a temperature gradient. The net heat produced in the conductor per unit volume per second can be written as:

$$\dot{Q} = \rho J^2 - \gamma J \frac{dT}{dl} \quad (1\text{-}4)$$

Where ρ is the electrical resistivity, J is the current density, γ is the Thomson coefficient, and $\frac{dT}{dl}$ is the temperature gradient along the conductor. The first term is independent of the temperature gradient, thus is the Joule heat, while the second term refers to Thomson heat.

γ, S and Π are related by the Kelvin relations:[3]

$$\gamma = T \frac{dS}{dT} \quad (1\text{-}5)$$

$$\Pi = TS \quad (1\text{-}6)$$

The equations above follow the energy conservation. A more rigorous way to derive the Kelvin relations can be derived based on modern solid state physics.[3,4]

Although the thermoelectric effects have been known for a long time, the devices widely utilized are thermocouples until recently. The thermocouples are used for temperature measurement and thermopiles. The theories of thermoelectric generators and refrigerators were developed by Altenkirch in 1909 and 1911, respectively.[5,6]

1-3. The figure of merit ZT and device efficiency.

Thermoelectric materials can be used for both electricity generation and refrigeration. It is important to evaluate the energy conversion efficiency. Figure 1-4 shows a typical thermoelectric unicouple with one p- and one n-type leg.
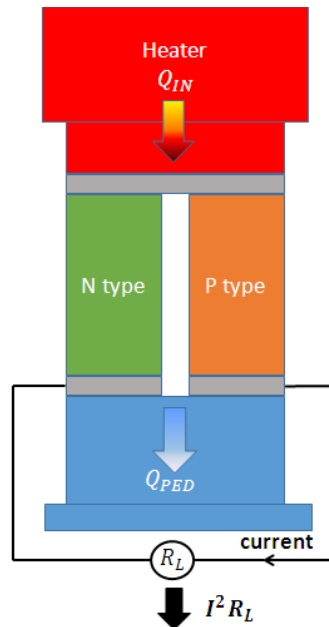
Figure 1-4. Schematic diagram of a one-stage TEG module.

The net heat absorbed or produced can be expressed in terms of the Peltier, Fourier, and Joule heat terms as:

$$Q = \left(S_p - S_n\right)T_c I - K(T_h - T_c) - \frac{1}{2}I^2 R \quad (1\text{-}7)$$

Where thermal conductance K and electrical resistance R are expressed as:

$$K = \frac{\kappa_n A_n + \kappa_p A_p}{L} \quad \text{(1-8)}$$

$$R = \frac{L}{\sigma_n A_n + \sigma_p A_p} \quad \text{(1-9)}$$

Where κ_n, A_n, σ_n are the thermal conductivity, cross-section area, and electrical conductivity for

n-type; κ_p, A_p, σ_p are the thermal conductivity, cross-section area, and electrical conductivity for

p-type.

The external power supply can be expressed as:

$$W = (S_p - S_n)(T_h - T_c)I + I^2 R \quad \text{(1-10)}$$

Thus, the conversion efficiency can be written as:

$$\eta = \frac{Q}{W} = \frac{(S_p - S_n)T_c I - K(T_h - T_c) - \frac{1}{2}I^2 R}{(S_p - S_n)(T_h - T_c)I + I^2 R} \quad \text{(1-11)}$$

The maximum efficiency is achieved when the following conditions are met:

$$\frac{A_p}{A_n} = \left(\frac{\kappa_p \sigma_p}{\kappa_n \sigma_n}\right)^{\frac{1}{2}} \quad \text{(1-12)}$$

$$IR = \frac{(S_p - S_n)(T_h - T_c)}{\sqrt{1 + ZT_M} - 1} \quad (1\text{-}13)$$

Where $T_M = (T_h + T_c)/2$, and $Z = \dfrac{(S_p - S_n)^2}{\left(\left(\frac{\kappa_p}{\sigma_p}\right)^{\frac{1}{2}} + \left(\frac{\kappa_n}{\sigma_n}\right)^{\frac{1}{2}}\right)^2}$

$$\eta_{max} = \frac{T_h}{T_h - T_c} \frac{\sqrt{1 + ZT_M} - 1}{\sqrt{1 + ZT_M} + \frac{T_c}{T_h}} \quad (1\text{-}14)$$

Z is called the figure of merit. Usually when referring the figure of merit to a thermoelectric material, Z is written as:

$$Z = \frac{S^2 \sigma}{\kappa} \quad (1\text{-}15)$$

It is clear that as Z rises, the conversion efficiency increases. High Z is expected to improve the conversion efficiency.

Figure 1-5 shows the dependence of normalized efficiency of a thermoelectric engine with respect to the figure of merit ZT. When ZT reaches 3 to 5, the conversion efficiency can be as high as 50% of the Carnot Engine, which is the typical efficiency of the conventional engine. So far, Bi-Te[7,8] and Pb-Te[9,10,11] series show the figure of merit to be above 1.5. The figure of merit leads to a 35% normalized efficiency approximately.
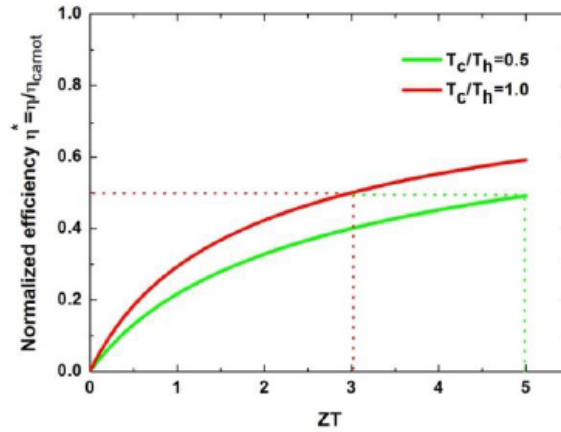
Figure 1-5. Normalized efficiency of TE engine vs. figure of merit ZT.

1-4. State of the art TE materials

As discussed in the previous section, the TE device will have a high efficiency if the figure of merit is large. According to the definition of figure of merit, an efficient TE material would have high thermopower, low electrical resistivity, and low thermal conductivity in the temperature range of interest. However, these conditions are not easy to be satisfied simultaneously. In most cases, the improvement of one property will contradict other conditions. Thus, the enhancement of figure of merit is limited. Wood *et al.* shows the ideal TE materials are semiconductors with the carrier concentrations in the range of 10^{19} to $10^{21}/cm^3$.[1] Figure 1-6 and figure 1-7 show the summary of some best ZT for both n-type and p-type bulk thermoelectric materials to date vs. temperature.[12]
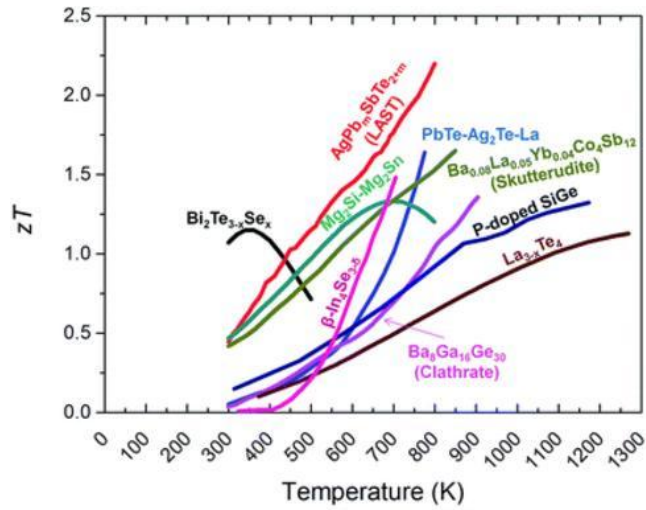
Figure 1-6. State-of-the-art n-type thermoelectric materials.
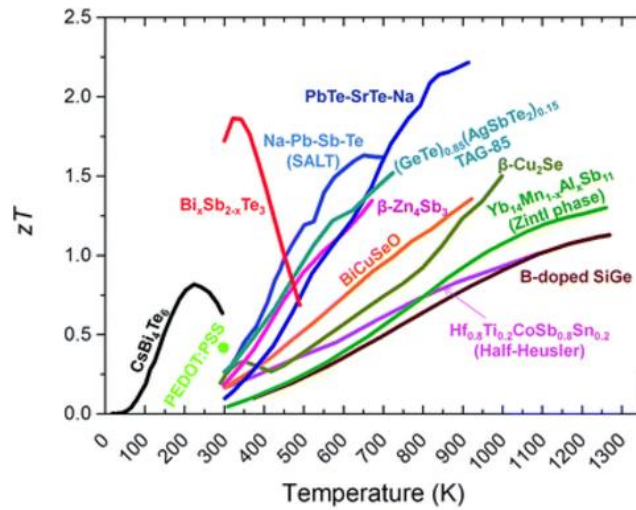
Figure 1-7. State-of-the-art p-type thermoelectric materials.

In the past decade, nanostructured engineering has been introduced to enhance the thermal properties of TE materials. Significant improvements on ZT have been reported in comparison with their bulk forms.[7,13-16]

To sum up, besides high figure of merit, the best candidates for thermoelectric device and future commercial should also have the following properties: their thermal stability and mass producibility.

1. Thermally stable at the operating temperatures.

2. Low-cost for mass producibility.

3. Non-toxic, toxic elements should be eliminated.

Half-Heusler alloys are good candidates satisfying the requirements above, and will be discussed in later chapters.

2. Sample synthesis and characterization.

2-1. Sample synthesis

2-1-1. Arc melting

Arc melting shown is a widely used method to melt elements with high melting points together and to form a homogeneous composite. Figure 2-1 shows the arc melting system. Most of the elements in our synthesis are ordered from Sigma Aldrich and Alfa Aesar with a purity of 99.5% or higher. The arc melting chamber is first pumped down to under 30 mTorr and then backfilled with argon. The argon works as protecting gas during melting process. During the melting process, a piece of Zirconium is melted first to consume the residual oxygen in the chamber. The ingot is flipped and melted three to four times to improve the homogeneity. For n-type half-Heusler XNiSn (X=Hf, Zr, Ti), a minute amount of Sb is added as an n-type dopant. Because Sb has a very low melting point compared to other high melting elements (Hf, Zr, Ti) in the composition, any loss of Sb during melting process will lead to a large deviation in the final composition. To solve this problem, we make a $Sn_{90}Sb_{10}$ alloy precursor first with a MAPP gas torch. The $Sn_{90}Sb_{10}$ has a much higher melting point than pure Sb, thus helps reducing the loss on Sb a lot.

Figure 2-1. Arc melting system.

2-1-2. Ball milling

Ball milling is the technique for powerful mechanical grinding and alloying. It is widely used to achieve nano-grain powders. The materials of ball milling vessels and balls are chosen based on the materials in order to reduce the contamination. For half-Heusler alloys, stainless steel vessels and ball set with two 0.25'' and four 0.125" in diameter balls are used. Based on experience, the ideal mass ratio of balls to samples is in the range between 6:1 and 8:1. After the elements are loaded in the vessel, it is then sealed and fixed in SPEX Dual ball miller 8000D. The ball miller is placed in an aluminum box. Ball milling process usually takes hours to get nano-size powders. Contamination level should be carefully checked as the ball milling time increases. The nanopowders achieved by ball milling are later compacted by using Spark Plasma Sintering (SPS).

2-1-3. Spark Plasma Sintering

Spark plasma sintering (SPS) is a powerful sintering technique. During sintering process, a DC current is generated and passes through the punches, die as well as the powders. In this way, the heat is generated to heat up and compact the sample. The SPS has a very high heating or cooling rate (up to 1000 K/min) compared to traditional methods, thus it is generally a very fast process. Even though the term "spark plasma sintering" is used, it is misleading, since no spark or plasma is involved in this technique.[17] Previous study has found that the grain size will increase fast as the sintering time is longer. So the rapid heating speed in SPS ensures that it has the potential to densify the powders while at the same time it avoids the significant grain growth during the sintering process.

Thermal Technologies SPS 10-4 model shown in Figure 2-2 is used for powder consolidation. The SPS has three main parts: a DC current supply, a hydraulic system for compressing, and an operating chamber. The consolidation process starts with loading the fine powders in a graphite die covered by a pair of graphite punches at both the top and bottom. A thin graphite foil is placed around the powders between the sample and the graphite die to avoid the contamination between the sample and the die. Then the die with powders is placed in the operating chamber between the upper and lower rams with the pressure of 5 MPa. Now it is ready to evacuate the chamber. Once the vacuum is as good as 2 mTorr, the sample is ready to heat up. The SPS has two heating systems: one is using a third thermal couple if the sintering temperature is below

1000 ℃. Otherwise, an infrared pyrometer is adopted to read the temperatures. A maximum heating rate of 300 K/min and pressure of 60 MPa are recommended for graphite. A usual sintering time ranges from a few minutes to one hour. After sintering, the obtained sample is covered by graphite foil. Following polishing is needed to get rid of the graphite.
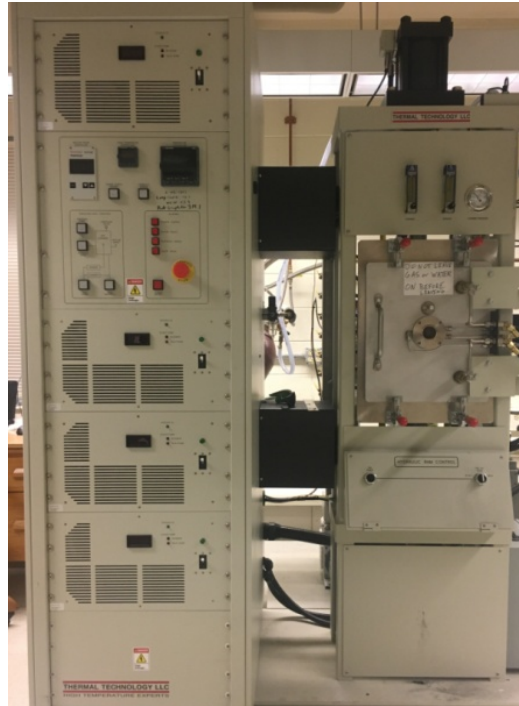
Figure 2-2. SPS 10-4 model made by Thermal Technologies.

2-2. Sample characterization

2-2-1. X-Ray Diffraction

X-Ray Diffraction (XRD) is a technique used to identify the crystalline structure. Half-Heusler disc is polished to a flat surface and placed in the PANalytical X'Pert Pro MPD instrument shown in Figure 2-3. This equipped with a Cu X-ray tube source. The diffracted beam has a Ni beta-filter and the scanning range is from 20° to 80° in diffraction angle. The obtained diffraction patterns are compared with the database to identify the possible phases and structures. XRD patterns can also be used to determine the stain level, which will be discussed in details in Chapter 3.
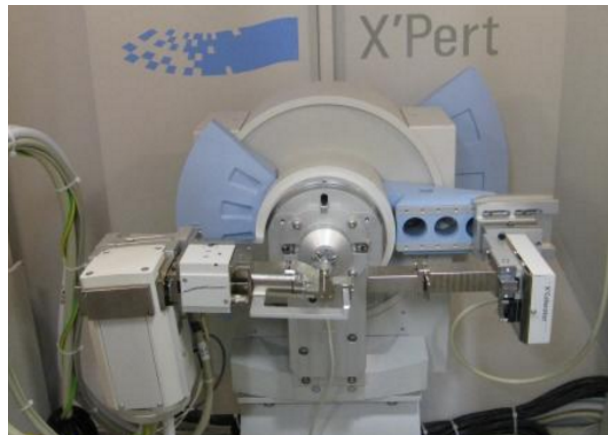
Figure 2-3. PANalytical X'Pert Pro MPD instrument.

2-2-2. Scanning Electron Microscope (SEM)

Scanning Electron Microscope is a type of microscope that can generate the images of a sample by scanning it with a focused beam of electrons. It can examine samples in both powder or bulk form. Powders are put on a piece of tape which is stick to the metal holder, while SEM micrographs are taken of the fractures located on the inside surface after breaking the samples in bulk form. Grain size distributions can be achieved based on the SEM images.

2-2-3. ZEM-3

ZEM-3 system by ULVAC-RIKO Inc is used to measure Seebeck coefficient and electrical resistivity. The measuring temperature range is from room temperature to 1000 °C and both Seebeck coefficient and electrical resistivity are measured simultanniously. A sample is inserted in a vertical position between two silver blocks. Gentle external pressure is applied to make sure good contact between sample and blocks. Electrical resistivity is measured by using the DC current four-terminal method. A DC current I is applied and passes through the silver blocks and the sample. Voltage across a pre-determined distance, ΔV, is measured. Then resistivity can be expressed as:

$$\rho = \frac{RL}{A} \quad (2\text{-}1)$$

Where R is the electrical resistance, L is the length between the two voltage leads, and A is the cross-sectional area of the sample. For Seebeck coefficient measurement, the sample is heated up

to a specified temperature by the heater in the lower silver block. Seebeck coefficient is measured by measuring the temperature difference $\Delta T = T_h - T_c$. Then the Seebeck voltage, ΔT_s, is read to determine the Seebeck coefficient.

Figure 2-4. ZEM-3 made by ULVAC-RIKO Inc.

2-2-4. Thermal conductivity measurement

The thermal conductivity κ can be calculated as:

$$\kappa = C_p D \alpha \quad (2\text{-}2)$$

Where C_p, D, and α are the specific heat capacity, density, and thermal diffusivity, respectively. Specific heat capacity is measured by Netzsch LFA Differential Scanning Calorimeter (DSC). This technique measures the difference in the amount of heat to increase the sample temperature

and reference as a function of temperature. It was firstly developed by Watson and O'Neill in 1962. The first adiabatic differential scanning calorimeter was used by Privalov and Monaselidz in 1964.[18] Density D is measured by Archimedes method. The diffusivity is measured by laser flash method in which an energy pulse is generated on one side of the sample. Then the detector detects how fast the energy reaches the backside of the sample. The faster the energy reaches the backside, the higher the thermal diffusivity is.

Another method for thermal conductivity measurement is time domain thermoreflectance (TDTR) (shown in Figure 2-5).[19-21] This method uses ultra-fast laser pulses to heat up the surface of a material system. Then a time delayed probe pulse is used to measure the change in the thermoreflectance of the surface due to the decay of the thermal energy deposited by the pump pulse. This change in thermorefectance can be utilized to derive the thermal conductivity.
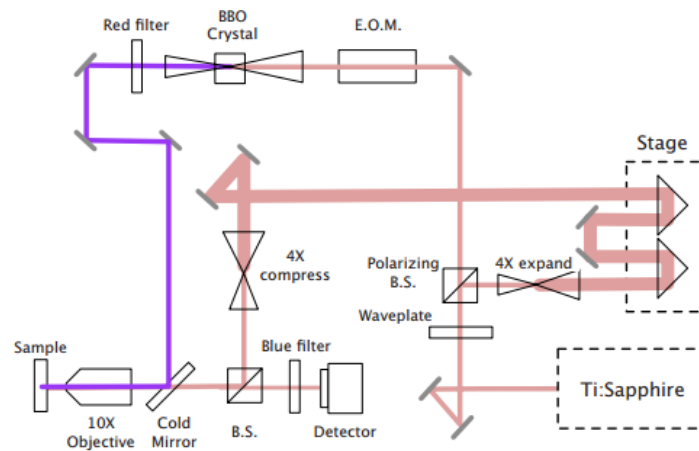
Figure 2-5. A schematic of the key elements of pump-probe system.

One important aspect of TDTR utilization is study the length dependent thermal conductivity. In order to probe various depths beneath the sample surface, the modulation frequency of the pump beam can be altered. The estimated depth is calculated as two time the thermal penetration depth, L_z which can be defined as the following:

$$L_z = 2\sqrt{\frac{\kappa}{\pi C_v f}} \quad (2\text{-}3)$$

When κ, C_v and f are the thermal conductivity, the volumetric heat capacity, and the modulation frequency, respectively.[22]

2-2-5. Hall Effect

The Hall effect measurement is conducted to help understand the characteristic property of the conductor. It reveals both carrier's type and concentration (n) as:

$$V_H = -\frac{IB}{nte} \quad (2\text{-}4)$$

$$R_H = \frac{V_H t}{IB} = -\frac{1}{ne} \quad (2\text{-}5)$$

Where V_H is the Hall voltage, R_H is the Hall coefficient, I is the current, B is the magnetic field, e is the carrier charge, and t is the thickness of the conductor in the direction of the magnetic

field. When a constant current passes through a conductor in a perpendicular magnetic field, the carriers will experience the Lorentz force and expose on the faces of the sample. This process will eventually to reach the equilibrim state where the induced electric field can completed balance the Lorentz force. The carrier mobility is obtained from combining the electrical conductivity and the carrier concentration as:

$$\mu_H = \frac{\sigma}{nq} \quad (2\text{-}6)$$

The Hall measurement is conducted on Quantum Design VersaLab.

3. Enhanced thermoelectric properties of Half-Heusler alloys

Half-Heusler (HH) alloys are promising thermoelectric (TE) materials due to their high thermopower and moderate electrical resistivity.[23-26] These alloys have composition XYZ, where X and Y denote transition or rare earth elements and Z denotes a main group element. In particular, the RNiSn-type HH alloys, where R = Hf, Zr, and Ti, are the most investigated to date due to their thermally stable[27] and mass producibility.[28] This chapter will focus on how to improve the thermopower and reduce the lattice thermal conductivity of half-Heusler alloys. The study of the relationship between the intrinsic disorder and thermoelectric properties of HH phases has gained attention recently.[29-32] Through proper annealing, there is an appreciable increase in power factor, decrease in charge carrier density, and increase in carrier mobility in previous (Hf, Zr)NiSn phase without the need of nanostructures. On the other hand by substituting proper elements and embedding nanoparticles in the HH matrix, the increase of thermopower and the reduction of thermal conductivity are observed. In addition, through introducing localized impurity states, the density of states of host at the Fermi level can be significantly increased, and it results in great enhancement of the Seebeck coefficient according to the Mahan-Sofo theory.

3-1. Improvement of structural order in Half-Heusler alloys

The crystal structure of HH alloys a face centered cubic (FCC). As shown in Figure 3-1, the transition metal M (M = Hf, Zr, Ti) atoms and Sn atoms form a rock salt frame, and four Ni atoms fill half of the eight quadrants. This is the reason why the term "Half Heusler" is used, compared with the term "Full Heusler" in which all eight quadrants are occupied.
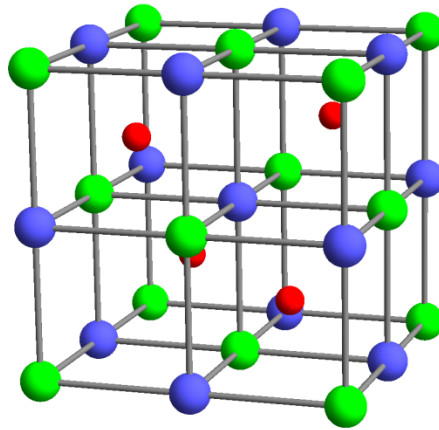
Figure 3-1. Crystal structure of MNiSn (M= Hf, Zr, Ti) half-Heusler phase.

3-1-1. Background

HH phases are prone to antisite disorder, as shown in Figure 3-2.[33-35] The intrinsic disorder can have an adverse influence on power factor, and thus ZT. ZT of HH phases has been at 1 at T~700-1100 K for a long time.[36-45] From the crystal chemistry viewpoint, antisite disorder seems inevitable.[29,33,34] There is a lot of effort in annealing samples significantly below the

melting point for long time to tackle this materials issue. But unfortunately antisite disorder is still persist even after the long-term annealing. The electronic structure that determines the band mass as well as the carrier mobility are very sensitive to lattice disorder. The intrinsic disorder that has plagued the TE performance of half-Heuslers can be reduced if the synthesis processes are carrier out near but below the melting temperatures. A significant enhancement of power factor is observed without the need of nanostructures or composition optimization. Correlations between structural order and thermoelectric properties are observed.
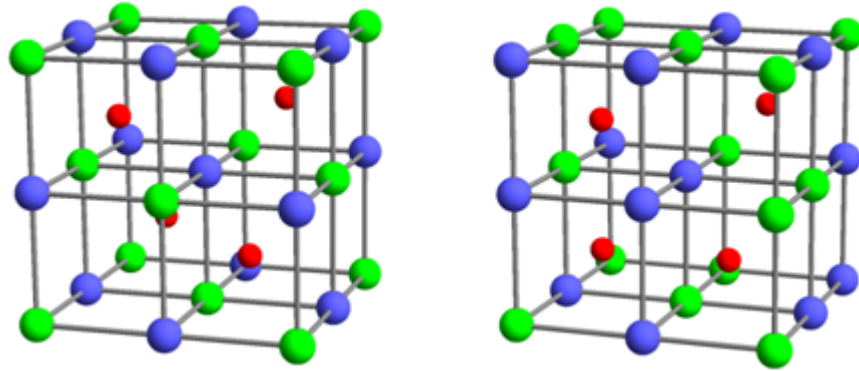
Figure 3-2. Half-Heusler unit cells with Hf, Zr (green), Sn (blue), and Ni (red) occupying three face centered-cubic sublattices. Left: the structure i perfectly ordered. Right: antisite disorder occurs between Sn and (Hf, Zr) atoms each of which have 4 atoms in the unit cell. Ni can occupy vacant fourth sublattice.

3-1-2. Experiments

$Hf_{0.6}Zr_{0.4}NiSn_{0.995}Sb_{0.005}$ is selected for investigation.[37] In order to focus on the issue of intrinsic disorder, the influence of any extrinsic effects must be minimized. Ti was deliberately excluded in order to avoid phase separation.[46] In contrast, the atomic size of Hf is the same as

that of Zr.[47,48] The ingot of $Hf_{0.6}Zr_{0.4}NiSn_{0.995}Sb_{0.005}$ was made by using arc melter with appropriate quantities of element Hf, Zr, Ni, Sn and pre-melted $Sn_{90}Sb_{10}$ alloy under argon atmosphere. Due to the low sublimation point of Sb element, the tiny amount of Sb might encounter a significant deviation from composite during melting process. One safe way to solve this issue was to make the $Sn_{90}Sb_{10}$ alloy in quartz tube with a hydrogen-oxygen torch. Ingot was then pulverized into 10 to 50 μm size powders followed by compacting in Spark Plasma Sintering (SPS) technique. The sintering temperature needed to achieve a fully dense compact was around 1100°C. Samples were sintered at 1100°C, 1250°C, and 1350°C for 30 minutes under 60 MPa. Microstructure and composition were investigated by using PANalyticalX'Pert Pro MPD instrument and FEI Quanta 650 Scanning Electron Microscope. Resistivity and thermopower measurements were performed using ZEM3 system. Thermal conductivity was calculated as the product of the specific heat (Netzsch Differential Scanning Calorimeter), the thermal diffusivity (Netzsch LFA 457 MicroFlash system) and the mass density. The lattice thermal conductivity $\kappa_L = \kappa - \kappa_e$ was obtained by knowing the electronic part of thermal conductivity κ_e, which is estimated by using the Wiedenann-Franz relationship $\kappa_e = L\sigma T$, where L is the Lorenz Number. The unique Lorenz number for each of the samples was determined by using the equation proposed by Kim *et al*. The Hall coefficient (R_H) was measured in a 1 T field using a Quantum Design physical property measurement system.

The as-cast ingots contained both HH phase as well as about 10-15% other phases. Systematic treatment of the ingots was conducted to obtain single-phase samples for characterization. For this study, samples were prepared as the following:

(i). One ingot was annealed at 700°C for 8 days;

(ii). One ingot was annealed at 1000°C for 2 days;

(iii). One disk was consolidated by using SPS sintering and annealing at 1100 $^{\circ}$C for 30 minutes;

(iv). One disk was consolidated by using SPS sintering and annealing at 1250 $^{\circ}$C for 30 minutes;

(v). One disk was consolidated by using SPS sintering and annealing at 1350 $^{\circ}$C for 30 minutes;

(vi). One disk was consolidated by using SPS sintering and annealing at 1400 $^{\circ}$C for 30 minutes;

(vii). One disk from (v) + additional annealing at 900°C for 2 days;

(viii). One disk from (v) + additional annealing at 900°C for 2 days.

The melting temperature of $Hf_{0.6}Zr_{0.4}NiSn_{0.995}Sb_{0.005}$ is around 1460°C [27]. For those temperatures significant below the melting temperature of the composition ((i) and (ii)), long term annealing is needed to obtain single phase because of the long-range atomic diffusion [23-26,49]. X-ray diffraction pattern for the annealed samples is shown in Figure 3-3. These peaks could be indexed to the half-Heusler phase, and on other phases were detected. For high temperatures ((iii), (iv), (v), and (vi)), atomic diffusion is much faster. (iii), (iv), and (v) are more homogeneous which is supported by the significant reduction in the lattice strain, but antisite

disorder may still exist in these cases. The sample annealed at 1400°C was partially melted and showed the appearance of about 10% secondary phases. Some reduction on strain in the HH phase was detected. (vii) and (viii) are made in order to further reduce the antisite disorder in the samples. It was found that the additional annealing has resulted in only a very small improvement on structural ordering.
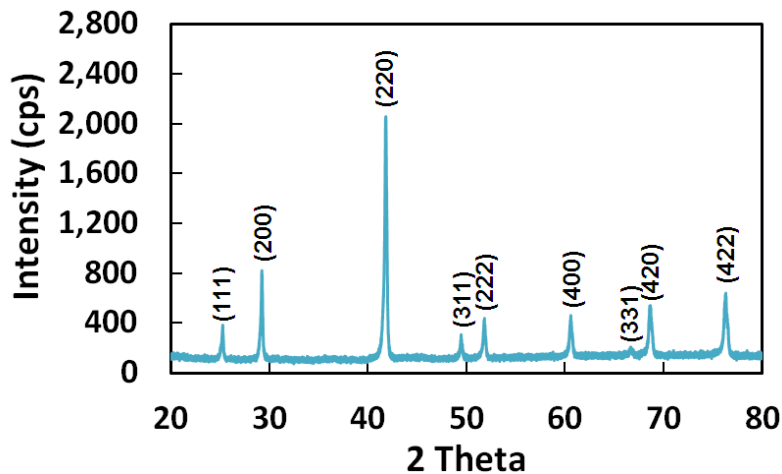
Figure 3-3. X-ray patterns for n-type Hf$_{0.6}$Zr$_{0.4}$NiSn$_{0.995}$Sb$_{0.005}$ ingot-based SPSed sample annealed at 700°C for 8 days. All samples annealed up to 1350°C show single-phase diffraction pattern.

The compositional homogeneity was checked by EDS map scan over a 90000 μm^2 area. No evidence for any compositional variation was found. The SEM micrographs for those samples annealed at: 700°C for 8 days, 1350°C for 30 minutes, and 1350°C for 30 minutes followed by 700°C for 8 days were shown in Figure 3-4 (a), (b) and (c) are. These SEM micrographs were taken of the fractures located on the inside surface after breaking the samples to determine the grain size. It shows that the grain size was found in the range of 100-400nm for the sample annealed at only 1350°C. For the sample annealed at 1350°C followed by 700°C, it had micron

size grains. The strain level and thermoelectric properties are similar for both the small and large grain size samples. This suggests that the most of the improvement in structural order has been achieved after annealing at $1350^{\circ}C$, and additional annealing at lower temperature is not helping reduce the strain level. Similar result was also observed for the sample annealed at $1350^{\circ}C$ followed by $900^{\circ}C$ for 2 days.
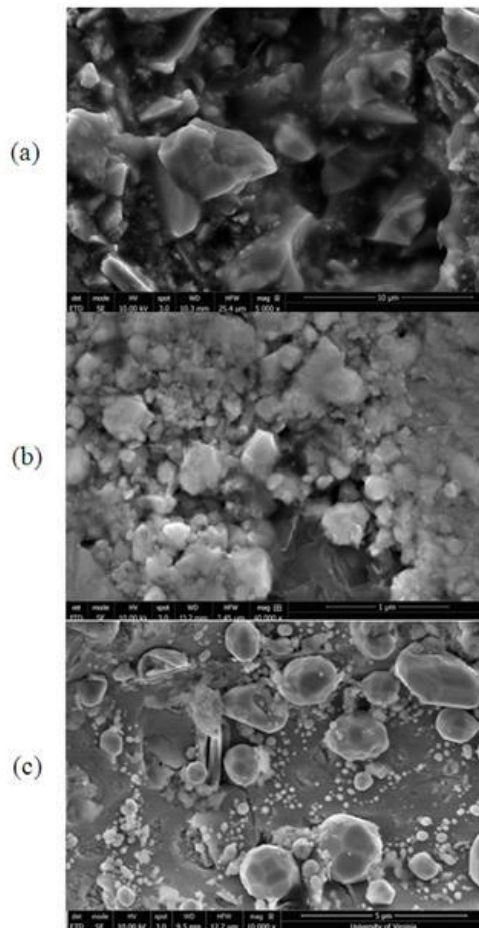
Figure 3-4. SEM micrographs for n-type $Hf_{0.6}Zr_{0.4}NiSn_{0.995}Sb_{0.005}$: (a) annealed at: $700^{\circ}C$ for 8 days, (b) annealed at $1350^{\circ}C$ for 30 minutes, (c) $1350^{\circ}C$ for 30 minutes followed by $700^{\circ}C$ for 8 days. Crystal facets can be clearly seen.

3-1-4. Discussion

In order to encode the degree of structural disorder, X-ray diffraction peak is conducted among the samples and the peak width is investigated. Peak widths are represented by the full width at half maximum (FWHM). FWHM and their uncertainties for different XRD patterns were determined by using Origin 8. To begin, HighScorePlus was used to determine the background of XRD patterns of the samples. The XRD pattern after deducting the background was fit using a joint combination of K-alpha and K-beta wavelengths. For these fittings, Lorentzian distribution was assumed for peak shape. The best fitting was achieved through minimizing the sum of the squared residuals. The K-beta peak was deducted from both experimental and fitting curves Fitting example was shown in Figure 3-5.
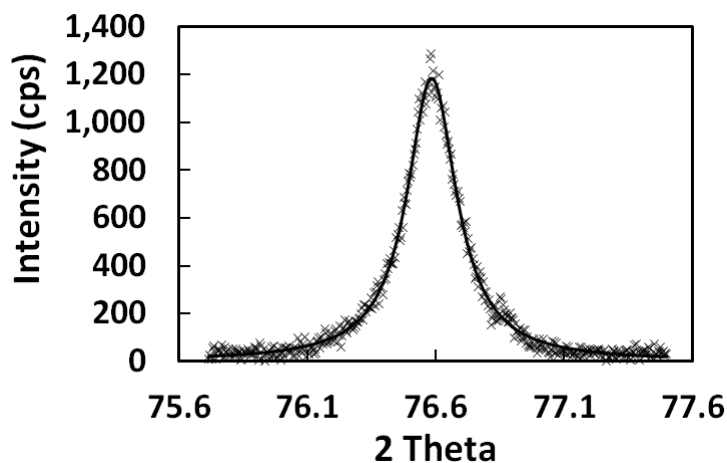
Figure 3-5. Experimental XRD (✕) and fitting curve (line) of peak (422) for $Hf_{0.6}Zr_{0.4}NiSn_{0.995}Sb_{0.005}$ annealed at $700^{o}C$ for 8 days. This is representative of the fitting for all peaks.

Peak width was then determined by calculating the FWHM for each fitting peak. Strains for different samples were achieved by using Scherrer's equation as the following:

$$\beta_t = \frac{0.9\lambda}{D\cos\theta} + 4\varepsilon\tan\theta + \beta_0 \quad (3\text{-}1)$$

Where β_t represents the total peak broadening coming from the contribution from average particle size (D), strain (ε) and instrumental broadening (β_0). λ is the wavelength, and θ is the diffraction angle [50]. In these half-Heusler samples, the average particle size was much larger than the wavelength, this term was eliminated from the analysis. Then strain could be determined by calculating the slope of FWHM as a function of $\tan\theta$ shown in Figure 3-6. The uncertainty of stain was determined by calculating the standard error of slope of linear fit of FWHM versus $\tan\theta$.
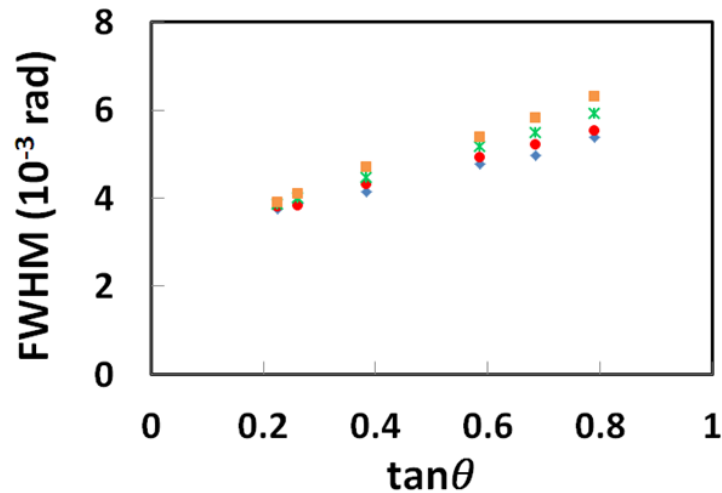
Figure 3-6. FWHM versus $\tan\theta$ for samples: SPS samples annealed at 1350ºC for 30 minutes (blue), 1250ºC for 30 minutes (red), and 1100ºC for 10 minutes (green); as cast ingot annealed at 700ºC for 8 days (orange).

The mark size represents the uncertainty of FWHM at specific tanθ. Experimental uncertainty is represented by the size of the data points.

Figure 3-7 shows the relationship between calculated lattice strain and the annealing temperature. We can see that the lattice strain does not change as the grain size increases from submicron to several microns. The measured lattice strain does not depend on the grain size and only depends on the annealing temperature. As the annealing temperature goes up, the lattice strain decreases. The degree of structural disorder is essentially encoded in the observed lattice strain.
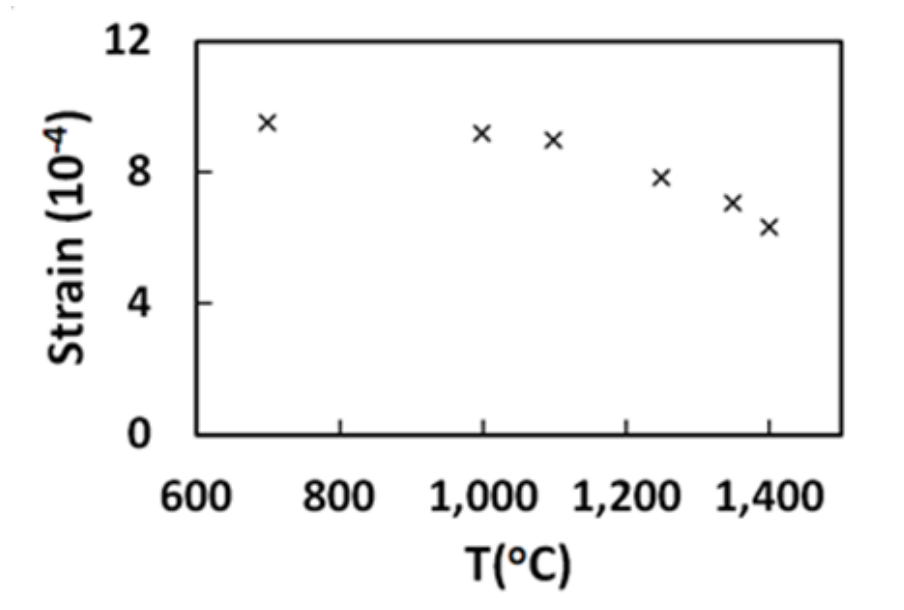
Figure 3-7. Lattice strain as a function of annealing temperatures for n-type $Hf_{0.6}Zr_{0.4}NiSn_{0.995}Sb_{0.005}$. Samples annealed at 1100°C and above are those prepared by using spark plasma sintering. Strain values for two samples annealed at 1350°C followed by additional annealing at 900°C and 700°C are similar to that for the sample annealed at only 1350°C. Experimental uncertainty is essentially represented by the size of the data points shown.

To investigate the thermoelectric properties of the HH samples annealing at different temperatures, $Hf_{0.6}Zr_{0.4}NiSn_{0.995}Sb_{0.005}$ samples annealed at 1350^oC, 1250^oC, 1100^oC, 1000^oC and 700^oC were examined. Figures 3-8a and 3-8b show that as the annealing temperature rises, the Seebeck coefficient increases over the entire temperature range. The electrical resistivity decreases when the annealing temperature goes up. The combination of increase in the Seebeck coefficient and the decrease in the electrical resistivity leads to a significant increase in the power factor ($PF = S^2/\rho$). Figure 3-9c shows that the power factor increases by as much as 50% as the annealing temperature increases from low temperature 700^oC to high annealing temperature of 1350^oC. Additional annealing of the 1350^oC-sample at lower temperatures resulted in negligibly tiny changes in both Seebeck coefficient and electrical resistivity. Though the significant growth in grain size was observed, the strain level did not change much as mentioned. The discovery of large increase in power factor is unprecedented for a monolithic half-Heusler alloy. For these samples, since it is absent of nanostructure, carrier trapping, which tends to enhance the thermopower, is not effective. Thus, the annealing temperature is the key role to benefit the electronic properties of the samples. Structural ordering must have an appreciable influence on the enhancement of PF.
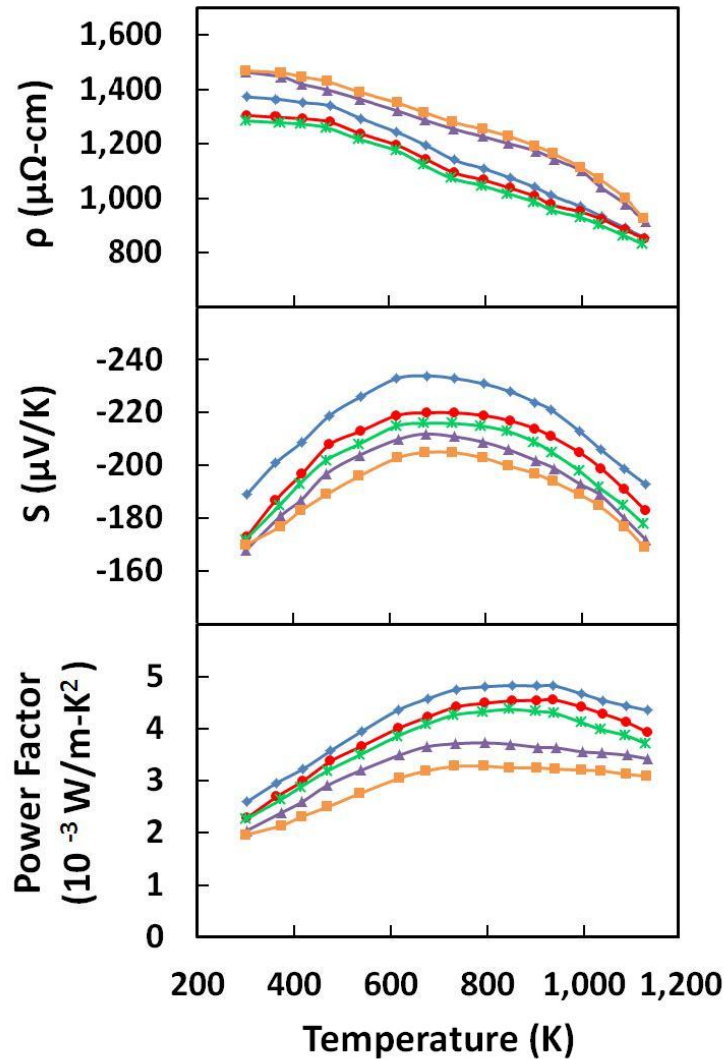
Figure 3-8. Thermoelectric properties of n-type $Hf_{0.6}Zr_{0.4}NiSn_{0.995}Sb_{0.005}$ annealed at 1350^oC for 30 minutes (blue rhombus), 1250^oC for 30 minutes (red circle), 1100^oC for 30 minutes (green star), 1000^oC for 2 days (purple triangle), 700^oC for 8 days (orange square): (a) Electrical resistivity (ρ), (b) Seebeck coefficient (S), and (c) Power Factor. Samples annealed at 1100^oC and above are those produced by the SPS method.

Given the large enhancement of power factor observed, the quest for high ZT is focused on the SPSed samples. These same samples show much higher dense, lower porosity and are much less likely to exhibit cracking than as cast samples. The thermal conductivity of the SPSed samples

were measured by using the laser flash technique. Thermal conductivity results of the samples are shown in Figure 3-9a and 9b. The total thermal conductivity and lattice thermal conductivity change little for the SPSed samples at different annealing temperatures, only by around 3% and 5%, respectively. Further, the variation of is not systematic according to temperature. The results also show the usual upturns at high temperatures. This observation can be attributed to bipolar contribution. Figure 3-9c shows figure of merit as a function of temperature. ZT increases from 1 to 1.2 for SPSed $Hf_{0.6}Zr_{0.4}NiSn_{0.995}Sb_{0.005}$. This increase in ZT is mostly due to increase in the power factor, resulting from the increase in the Seebeck coefficient and decrease in electrical resistivity.
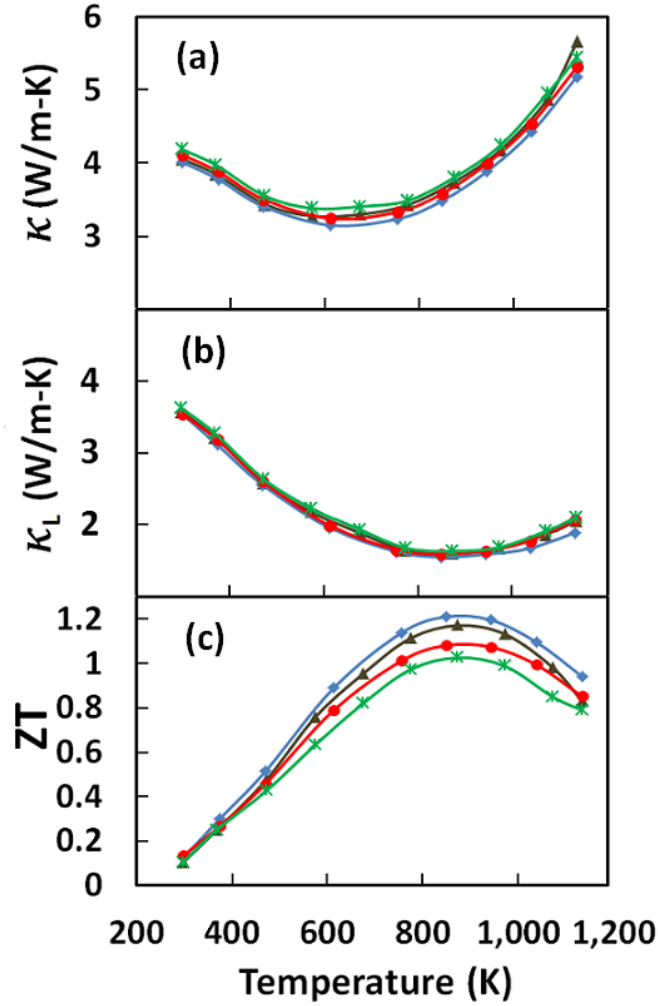
Figure 3-9. (a) Thermal conductivity (κ), (b) lattice thermal conductivity (κ_L), and (c) ZT of n-type Hf$_{0.6}$Zr$_{0.4}$NiSn$_{0.995}$Sb$_{0.005}$ annealed at 1350°C for 30 minutes (blue rhombus), 1250°C for 30 minutes (red circle), 1100°C for 30 minutes (green star), 1350°C for 30 minutes followed by 700°C for 8 days (dark brown triangle). Given the uncertainty in all the measurements, the resulting ZT has an uncertainty of $\approx$ ±10%, which is comparable or less than most other groups.

The electronic origin of the enhanced power factor was investigated by the Hall effect measurements. As mentioned in Chapter 2, the Hall coefficient ($R_H = -1/nq$) reveals both the carrier type and carrier density, where n is the carrier concentration and q the carrier charge. The

42

carrier mobility (μ_H) is then achieved from the electrical conductivity which is defined as the following:

$$\sigma = nq\mu_H \quad (3\text{-}2)$$

Previous investigation showed that the electronic transport properties of n-type (Hf,Zr)NiSn half-Heusler alloys could be described by a single-band model [51]. The n and μ_H values determined for the one-band model are shown in Table I. The values show that as annealing temperature increases, n decreases and thus, μ_H increases. After applying the Mott formula to a degenerate semimetal at temperatures below the Fermi temperature [52], the thermopower can be expressed as the scaling relation:

$$S \sim qm^*T/n^{2/3} \quad (3\text{-}3)$$

where m* is the effective band mass. This relation shows as the S increases, the carrier concentration decreases. This was observed. The carrier concentration decreases by as much as a factor of near three across the samples. This is correlated with the decrease in the lattice strain. Correspondingly, the carrier mobility μ_H rises by nearly a factor of three. As the structural order improves, it also helps enhance the semiconducting state of the half-Heusler phase. Previous studies have alluded to certain imperfections inside the bandgap manifested in the presence of in-gap states and thus a reduced bandgap size is observed [29,53,54]. The bandgap can be achieved by using the expression given by Goldsmid and Sharp as the following:

$$E_g = 2e|S_{max}|T_{max} \quad (3\text{-}4)$$

Where E_g is the bandgap, $|S_{max}|$ is the magnitude of the maximum thermopower, and T_{max} is the temperature at which $|S_{max}|$ occurs [55]. The band gap E_g values of the samples are shown in Table 1. It shows that as the annealing temperature increases, a systematic enhancement in the bandgap is observed. The bandgap for these alloys has been estimated to be in the range 0.18-0.50eV which is comparable to previous studies [53,56].

Condition	Hall coefficient R_H ($10^{-1}cm^3$/C)	Carrier concentration n ($10^{19}cm^{-3}$)	Hall mobility μ_H (cm^2/(V*s))	Band gap E_g (eV)
Anneal 700°C, 8 days	-2.21	2.83	15.1	0.276
Anneal 1000°C, 2 days	-3.45	1.81	24.0	0.284
SPS:1150°C	-3.47	1.80	27.1	0.286
SPS:1250°C	-3.57	1.75	28.3	0.298
SPS:1350°C	-5.17	1.21	38.2	0.317
SPS:1350°C anneal 700°C, 8 days	-5.39	1.16	38.3	0.316
SPS:1350°C anneal 900°C, 2 days	-5.43	1.15	40.1	0.319

TABLE I. Hall coefficient (R_H), carrier concentration (n), Hall mobility (μ_H) and and Band gap (E_g) of Hf$_{0.6}$Zr$_{0.4}$NiSn$_{0.995}$Sb$_{0.005}$ under different synthesis and annealing conditions. Samples prepared by SPS were annealed for 30 minutes at the temperatures shown.

3-1-5. Conclusions of improving the structural orders

In this work, thermoelectric properties of n-type (Hf,Zr)NiSn half-Heusler alloys have been investigated by annealing the materials near the melting point in order to improve the structural order. This is supporting by the evidence of the reduction in the lattice strain. The enhancement of the structural order has led to a significant increase in the power factor, by as much as 50%, very tiny change in thermal conductivity, thus resulted in the increase of ZT to 1.2 from 1 without the need of nanostructures in these samples. The large increase in power factor was attributed to the significant increase of carrier mobility and decrease of charge carrier density. This observation is consistent with the strengthening of the bandgap of the half-Heusler phase. This approach is not limited to any specific compositions. If applied to the broader class of Heusler alloys, it may help result in the enhancement of their multifunctional properties.

3-2. Improvement of TE properties through elemental substitution and embedment of nanoparticles

3-2-1. Mass fluctuation Effect on Lattice thermal conductivity

To analyze the mass fluctuation effect, we should recall the impurity scattering term of relaxation time as $\tau_i^{-1} = A\omega^4$. According to what Callaway [57] and Klemens [58] proposed, the constant A can be written as:

$$A = \frac{V_0}{4\pi c^3} \sum_i f_i (M_i - M)^2 \quad (3\text{-}5)$$

Where V_0, f_i, M_i, and M are the volume per atom, the fraction of atoms with mass M_i, the mass of atom i, and the average atom mass, respectively. For a two-phase heterogeneous system, A is expressed as [59]:

$$A = \frac{V_0}{4\pi c^3} (1-x)x \left(\frac{M_1 - M_2}{M}\right)^2 \quad (3\text{-}6)$$

Where x is the ratio of constituents in the system. To achieve the lowest lattice thermal conductivity based on mass fluctuation effect, the ratio of constituents can be optimized. In n-type half-Heusler $Hf_{0.6}Zr_{0.4}NiSn_{0.995}Sb_{0.005}$, the atom sizes of Hf and Zr atoms are larger than Ti atom. The mass fluctuation parameter A should increase if some of the Hf and Zr atoms are replaced by Ti atom. In this way, a decreased lattice thermal conductivity would be expected.

3-2-2. Thermopower enhancement via energy filtering

It is believed that low energy charge carriers are detrimental to the Seebeck coefficient. Moyzhes and Nemchinsky proved that the carrier with energy lower than its chemical potential will have an opposite contribution to thermopower compared to the carrier with energy whose energy is higher than its chemical potential. Thus the total thermopower will be lower if a system contains carrier with both kinds. If the carriers with low energy can be effectively scattered, an enhanced thermopower is expected. Adding ZrO_2 in n-type half-Heusler $Hf_{0.6}Zr_{0.4}NiSn_{0.995}Sb_{0.005}$, a higher Seebeck coefficient was observed as expected. ZrO_2 not only helps filter carriers with low energy, on the other hand, it also serves as scattering center, as evident of the increased resistivity. The higher resistivity helps reduce the electronic part of thermal conductivity, resulting in a very promising figure of merit for TE generators.

3-2-3. Sample synthesis

Ingots of $Hf_{0.6}Zr_{0.4}NiSn_{0.995}Sb_{0.005}$ and $Hf_{0.6}Zr_{0.25}Ti_{0.15}NiSn_{0.995}Sb_{0.005}$ were made by using arc melter from the appropriate quantities of elemental Hf, Zr, Ti, Sn and pre-melted $Sn_{90}Sb_{10}$ alloy under argon atmosphere. The reason of using a Sn-Sb alloy instead of elemental Sb in the alloying process was discussed in the previous section. The ingots then were pulverized into fine powders of around 10 to 50 μm in sizes. Then, both $Hf_{0.6}Zr_{0.4}NiSn_{0.995}Sb_{0.005}$ and $Hf_{0.65}Zr_{0.25}Ti_{0.15}NiSn_{0.995}Sb_{0.005}$ powders were mixed with 2 vol% ZrO_2 nano-particles by using

ball miller for 5 minutes. The powders with and without ZrO_2 nano-particles were then consolidated by using Spark Plasma Sintering (Thermal Technologies SPS 10-4) technique. These $Hf_{0.6}Zr_{0.25}Ti_{0.15}NiSn_{0.995}Sb_{0.005}$ samples were first sintered at a lower temperature of 1300 °C for 15 min under 60 MPa to ensure that a single phase was formed in the mixed-phase ingots before the SPS went to higher temperature. Then additional annealing at a higher temperature was performed at 1350 °C for another 15 min. On the other hand, the $Hf_{0.6}Zr_{0.4}NiSn_{0.995}Sb_{0.005}$ samples were known to have higher melting points (Hf and Zr have higher melting points than Ti), and they were sintered directly at 1350 °C for 30 min under 60 MPa. To confirm the phases of samples, an X-ray diffraction analysis was performed using the PANalyticalX'Pert Pro Multi-Purpose Diffractometer (MPD) instrument in air at room temperature on each of the sample. The sample composition and microstructure was investigated using FEI Quanta 650 Scanning Electron Microscope. Both the electrical resistivity and thermoelectric power were measured together by a four-probe method on ZEM3 system. The thermal conductivity was then calculated from the specific heat C_p (Netzsch Differential Scanning Calorimeter), the thermal diffusivity α (Netzsch LFA 457 MicroFlash system), and the sample density D as $\kappa = C_p \alpha D$. The lattice thermal conductivity $\kappa_L = \kappa - \kappa_e$ can be achieved by knowing κ_e, where κ_e is the electrical contribution that can be estimated by using the Wiedenann-Franz relationship $\kappa_e = L\sigma T$, where L is the Lorenz Number. The unique Lorenz number for each of the samples was determined by using the equation proposed by Kim *et al.*[60].

3-2-4. Discussion

The X-ray patterns of $Hf_{0.6}Zr_{0.25}Ti_{0.15}NiSn_{0.995}Sb_{0.005}$ with 0% and 2% ZrO_2 nanoparticle inclusions can be indexed to HH structure (space group F$\underline{4}$3m, C1$_b$), shown in Figure 3-10. In this pattern, an impurity phase can also be identified as ZrO_2 in the n-type alloy dispersed with ZrO_2 nanoparticle inclusions. The compositional homogeneity checked by energy dispersive spectroscopy map scanning over an area of 10000 μm^2 shows no evidence for any compositional variation or other phases. In addition, previous study has been done on the calculation of the binodal and spinodal curves in the isopleths TiNiSn-ZrNiSn and TiNiSn-HfNiSn. Based on the calculation, the SPS temperature of 1350 ^{o}C for our $Hf_{0.65}Zr_{0.25}Ti_{0.15}NiSn_{0.995}Sb_{0.005}$ samples is sufficiently high above the calculated critical point in order to achieve single phase in term of the Ti content. The typical main matrix of our samples has micron size grains, while for nanoclusions, they vary from 70 to 250 nm. Those grain sizes values are similar to those reported earlier [37].
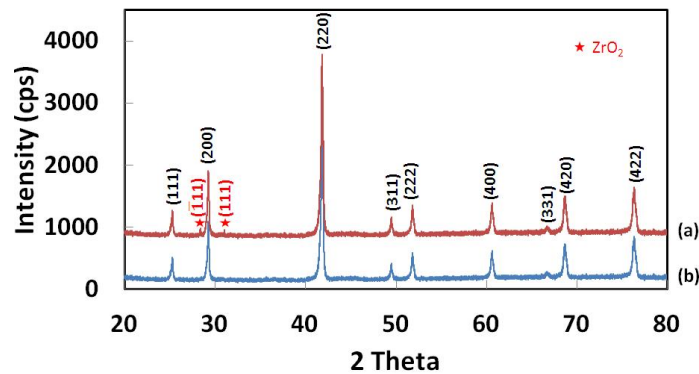

Figure 3-10 X-ray patterns of n-type $Hf_{0.6}Zr_{0.25}Ti_{0.15}NiSn_{0.995}Sb_{0.005}$ embedded with (a) 2% and (b) 0% ZrO_2 nanoparticles.

The temperature dependences of the electrical resistivity ρ, the Seebeck coefficient S, and the power factor are shown in Figure 3-11. It can be seen from the figure that all the $Hf_{0.6}Zr_xTi_{0.4-x}NiSn_{0.995}Sb_{0.005}$ compounds that contain or do not contain ZrO_2 nanoparticles show n-type behavior, as evident by the negative values of the Seebeck coefficient. As we replaced 15% Zr with Ti and added ZrO_2 nanoparticles, the resistivity increases over the entire temperature range. The Seebeck coefficient increases as the temperature rises from room temperature, and then starts to decrease for each sample. The maximum of the Seebeck coefficient is reached at about 780K. The increase of the Seebeck coefficient by the addition of ZrO_2 nanoparticles serving as potential barriers (discussed in the previous session) for carrier scattering is also observed among these samples. The Hall coefficient ($R_H= -1/nq$) reveals both the carrier type and carrier concentration, where n is the carrier concentration and q is the carrier charge. The carrier mobility is then deduced from the relation $(\sigma = nq\mu_H)$, where σ is the electrical conductivity. The estimated errors for carrier concentration and mobility by Hall measurement are 10%. To estimate the effective band mass, the formulas below are used by assuming a one-band model with acoustic phonon scattering [61]:

$$S = \pm \frac{k_B}{e}\left[\frac{2F_1(\eta_F)}{F_0(\eta_F)} - \eta_F\right] \quad (3\text{-}7)$$

$$F_n(\eta_F) = \int_0^\infty \frac{x^n}{1+e^{(x-\eta_F)}}dx \quad (3\text{-}8)$$

$$n = \frac{4}{\pi}\left(\frac{2\pi m^* k_B T}{h^2}\right)^{\frac{3}{2}}F_{1/2}(\eta_F) \quad (3\text{-}9)$$

Where $F_n(\eta_F)$ is the Fermi-Dirac integral, η_F is the reduced Fermi level defined as $\eta_F = E_F/k_B T$, k_B is the Boltzmann constant, m^* is the effective band mass. h is the Planck constant, and T is the temperature in the unit of K. The use of the single-band model for the above analysis was justified by previous study on the same system of materials [51]. Table II shows the n, μ_H, and calculated m^* values. The effective band mass for these alloys has been estimated to be larger than $2m_e$, which is consistent with previous studies [32, 51]. It shows that n decreases and μ_H increases after substituting Ti and adding ZrO_2 to the samples. The decrease of n may be attributed to bandstructure effect in the case of alloying and charge trapping in the case of nanoparticles embedment. A plausible reason for the increase of carrier mobility could be due to the decrease in carrier scattering as n decreases. The thermal power can be written in terms of the scaling relation $S \sim qm^*T/n^{2/3}$ after applying the Mott formula at temperature below the Fermi Temperature [62]. This relation reveals that the Seebeck coefficient increases as n decreases, that is observed. Despite of the enhancement of S, power factor, $PF=S^2/\rho$, of the samples with Ti or ZrO_2 nanoparticles remain similar compared with $Hf_{0.6}Zr_{0.4}NiSn_{0.995}Sb_{0.005}$ samples due to the increase in ρ.
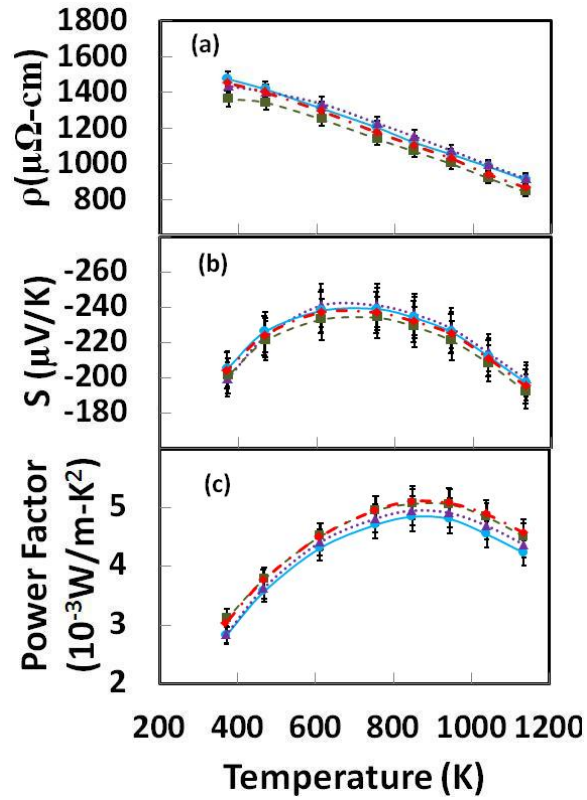
Figure 3-11 Thermoelectric properties of n-type Hf$_{0.6}$Zr$_{0.4}$NiSn$_{0.995}$Sb$_{0.005}$ (dashed line with green square), Hf$_{0.6}$Zr$_{0.4}$NiSn$_{0.995}$Sb$_{0.005}$/nano-ZrO$_2$ (dash dotted line with red rhombus), Hf$_{0.65}$Zr$_{0.25}$Ti$_{0.15}$NiSn$_{0.995}$Sb$_{0.005}$ (solid line with blue circle), Hf$_{0.65}$Zr$_{0.25}$Ti$_{0.15}$NiSn$_{0.995}$Sb$_{0.005}$/nano-ZrO$_2$ (round dotted line with purple triangle): (a) Electrical resistivity (ρ), (b) Seebeck coefficient (S), and (c) Power Factor.

Composition	R_H $(10^{-1}cm^3/C)$	n $(10^{19}cm^{-3})$	μ_H $(cm^2/(V*s))$	m^* (m_0)
Hf$_{0.6}$Zr$_{0.4}$NiSn$_{0.995}$Sb$_{0.005}$	-5.17	1.21 ± 0.12	38.2 ± 3.8	2.53
Hf$_{0.6}$Zr$_{0.4}$NiSn$_{0.995}$Sb$_{0.005}$+2%ZrO$_2$	-5.34	1.17 ± 0.12	38.4 ± 3.8	2.49

$Hf_{0.6}Zr_{0.25}Ti_{0.15}NiSn_{0.995}Sb_{0.005}$	-5.73	1.09 ± 0.11	38.9 ± 3.9	2.62
$Hf_{0.6}Zr_{0.25}Ti_{0.15}NiSn_{0.995}Sb_{0.005}+2\%ZrO_2$	-5.85	1.07 ± 0.11	40.7 ± 4.1	2.56

Table II. Hall coefficient (R_H), carrier concentration (n), Hall mobility (μ_H), and effective band mass (m^*) of $Hf_{0.6}Zr_{0.4}NiSn_{0.995}Sb_{0.005}$ and $Hf_{0.65}Zr_{0.25}Ti_{0.15}NiSn_{0.995}Sb_{0.005}$ embedded with 0% and 2% ZrO_2 samples.

Thermal conductivity results of these samples are shown in Figure 3-12a. It shows that the value of the thermal conductivity decreases with the substitution of Ti and addition of ZrO_2 nanoparticles in the compositions. The lattice thermal conductivity κ_L shown in Figure 3-12b was calculated from the relation $\kappa_L = \kappa - \kappa_e$. It reveals that the lattice thermal conductivity decreases after substituting (Hf, Zr) with Ti and adding ZrO_2 nanoparticles in the compositions. The decrease of the lattice thermal conductivity comes from the mass fluctuation scattering resulting from the substitution of (Hf, Zr) by Ti and the ZrO_2 nanoparticles serving as scattering centers.
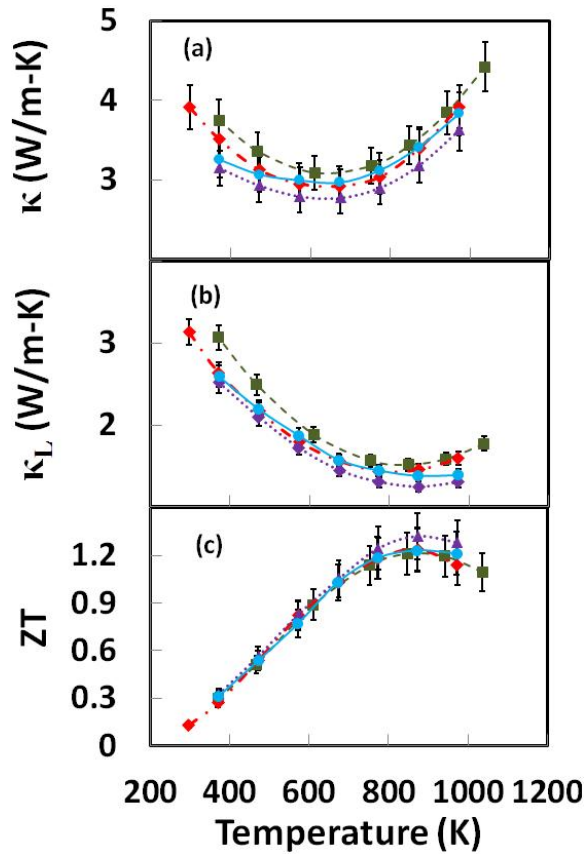
Figure 3-12 (a) Thermal conductivity (κ), (b) lattice thermal conductivity (κ_L), and (c) Figure of merit *ZT* of n-type Hf$_{0.6}$Zr$_{0.4}$NiSn$_{0.995}$Sb$_{0.005}$ (dashed line with green square), Hf$_{0.6}$Zr$_{0.4}$NiSn$_{0.995}$Sb$_{0.005}$/nano-ZrO$_2$ (dash dotted line with red rhombus), Hf$_{0.65}$Zr$_{0.25}$Ti$_{0.15}$NiSn$_{0.995}$Sb$_{0.005}$ (solid line with blue circle), Hf$_{0.65}$Zr$_{0.25}$Ti$_{0.15}$NiSn$_{0.995}$Sb$_{0.005}$/nano-ZrO$_2$ (round dotted line with purple triangle). Given the uncertainty in all the measurements, the resulting *ZT* has an uncertainty of $\approx \pm 10\%$, which is comparable or less than most other groups.

Due to the appreciable decrease of thermal conductivity by the substitution of (Hf, Zr) by Ti and addition of ZrO$_2$ in the compositions, the figure of merit *ZT* increases despite the slight decrease of the power factor, as shown in figure 3-12(c). The maximum *ZT* values for Hf$_{0.6}$Zr$_{0.4}$NiSn$_{0.995}$Sb$_{0.005}$ and Hf$_{0.6}$Zr$_{0.25}$Ti$_{0.15}$NiSn$_{0.995}$Sb$_{0.005}$ are about 1.21 and 1.23 at 750K

respectively and increase to 1.24 and 1.32 at 750K as a result of adding ZrO_2 nanoparticles. The measurement uncertainties are estimated to be 3% for ρ, α, and C_p and 5% for S, respectively. As a result, the resulting ZT contains 10% uncertainty, which is the same as that reported by Yan *et al.*

3-2-5. Conclusion

In this work, thermoelectric properties of the substitution of Ti for (Hf, Zr) sites and the addition of nano-ZrO_2 in (Hf, Zr)NiSn are investigated. Due to enhanced phonon scattering by Ti substitution and embedded nanoparticles, thermal conductivity is significantly reduced for (Hf, Zr)NiSn. In addition, ZrO_2 nanoparticles serve as potential barriers for carrier scattering that help improve the thermopower. All of these led to a maximum ZT value of 1.3 at around 850K for $Hf_{0.6}Zr_{0.25}Ti_{0.15}NiSn_{0.995}Sb_{0.005}$/nano-$ZrO_2$ without the need of nanostructured HH phases.

3-3. Power conversion efficiency model

As we have discussed in Chapter 1, device efficiency was calculated using a temperature-averaged figure of merit (ZT) previously [63,64]. However, that is inadequate since all the relevant TE parameters are temperature dependent. Furthermore, the TE parameters for the n-leg and p-leg are also different. In this part, the device efficiency is derived and calculated using the

temperature dependent parameters for the n-leg and p-leg of a couple module assuming one thermoelectric unicouple with one p- and one n-type leg which is shown in Figure 3-13.
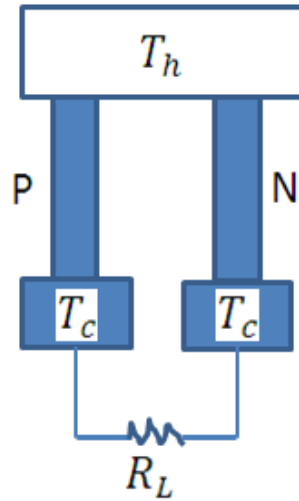
Figure 3-13. A schematic diagram of a one-stage TEG module.

For Seebeck coefficient, it is the induced thermoelectric voltage in response to a temperature difference across the materials. Thus, when accumulating open circuit voltage, no matter what the position-dependent Seebeck coefficient is, the voltage is the integration of the known temperature-dependent Seebeck coefficient ($S(T)$) over the temperature range-from cold-side temperature (T_h) to hot-side temperature (T_c).

$$\text{Open circuit voltage: } V_{oc} = \int_{T_c}^{T_h} S(T)dT = \int_{T_c}^{T_h} (S_p(T) - S_n(T))dT \quad \text{(3-10)}$$

$$\text{Current: } I = {V_{oc}} \big/ {(R_L + R_n + R_p)} \quad \text{(3-11)}$$

$$\text{Output power: } P = I^2 R_L \quad (3\text{-}12)$$

Where L is the length of pellet, A is the cross sectional area of pellet.

The input heat power to the TE generator:

$$\dot{Q}_h = \dot{Q}_P + \dot{Q}_F + \dot{Q}_J \quad (3\text{-}13)$$

Where $\dot{Q}_P$, $\dot{Q}_F$, and $\dot{Q}_J$ are the Peltier, Fourier, and Joule heat terms, respectively.

The rate of the change of Peltier heat is given by the following equation:

$$\dot{Q}_P = S_h I T_h \quad (3\text{-}14)$$

Where S_h is the Seebeck coefficient at the hot-side temperature T_h. To determine the rate of the change of Fourier heat $\dot{Q}_F$, the pellet is split into many small sub-sections.

Starting from the energy balance in the system:

$$\frac{dE}{dt} = -\nabla \cdot \vec{q} + g(\vec{r}, t) \quad (3\text{-}15)$$

Where $\frac{dE}{dt}$ is the rate of change of heat content per unit volume of materials, $-\nabla \cdot \vec{q}$ represents the rate of change of the net outflow of thermal energy through the unit volume, and $g(\vec{r}, t)$ is the rate of internal heat generation/absorption at a point in the body.

For p-type HH material, in this single pellet steady-state case, the rate of change of heat content is time-independent, and the internal heat generation/absorption is zero. In addition we assume that the heat flows in the x-direction, thus the following relation can be achieved:

$$\nabla \cdot \vec{q} = \frac{\partial q_{x(T)}}{\partial x(T)} = \frac{\partial (k_p(x(T)) \frac{\partial T}{\partial x(T)})}{\partial x(T)} = 0 \quad (3\text{-}16)$$

To solve the differential equation above, first we can get:

$$k_p(x(T)) \frac{\partial T}{\partial x(T)} = Constant \quad (3\text{-}17)$$

Since x is temperature dependent, $k(x) = k(T)$, and we know the expression of $k(T)$ by fitting the experimental data, we can determine the relationship between T and x by solving (3-17):

$$\int_{T_c}^{T} k_p(T) dT = \int_0^x Constant\, dx \quad (3\text{-}18)$$

$$x(T) = \frac{1}{Constant} \int_{T_c}^{T} k_p(T) dT \quad (3\text{-}19)$$

To determine the Constant, the temperature-dependent thermal conductivity is continuously differentiable on each single temperature point in the measured range. The unknown constant can be achieved:

$$Constant = \frac{1}{L} \int_{T_c}^{T_h} k_p(T)dT \quad (3\text{-}20)$$

The Fourier heat term $\dot{Q}_F$ can be written as:

$$\dot{Q}_{F,p} = \int_{T_c}^{T_h} \frac{1}{R_{thermal,p}} dT \quad (3\text{-}21)$$

The accumulated thermal resistance $R_{thermal,p}$ can be determined as:

$$R_{thermal,p} = \int_0^L \frac{dx(T)}{k_p(x(T))*A} \quad (3\text{-}22)$$

Since $x(T = \frac{1}{Constant} \int_{T_c}^{T} k_p(T)dT$, where $Constant = \frac{1}{L} \int_{T_c}^{T_h} k_p(T)dT$

$$dx(T) = \frac{dx(T)}{dT} dT \quad (3\text{-}23)$$

$$\frac{dx(T)}{dT} = \frac{1}{Constant} * \frac{d\left(\int_{T_c}^{T} k_p(T)dT\right)}{dT} = \frac{k_p(T)}{Constant} \quad (3\text{-}24)$$

Combining (3-22)-(3-24) together, the accumulated thermal resistance $R_{thermal,p}$ can be further written as:

$$R_{thermal,p} = \int_0^L \frac{dx}{k_p(x)*A} = \int_{T_c}^{T_h} \frac{1}{k_p(T)*A} * \frac{k_p(T)}{Constant} dT = \frac{L*(T_h-T_c)}{A*\int_{T_c}^{T_h} k_p(T)dT} \quad (3\text{-}25)$$

Then, the Fourier heat term $\dot{Q}_{F,p}$ is expressed as:

$$\dot{Q}_{F,p} = \int_{T_c}^{T_h} \frac{1}{R_{thermal,p}} dT = \int_{T_c}^{T_h} k_n(T) * \frac{A}{L} dT \quad (3\text{-}26)$$

Similarly we can get $\dot{Q}_{F,n} = \int_{T_c}^{T_h} \frac{1}{R_{thermal,n}} dT = \int_{T_c}^{T_h} k_n(T) * \frac{A*\theta}{L} dT$

The total Fourier heat term $\dot{Q}_F$ is the sum of that of both n-type and p-type legs:

$$\dot{Q}_F = \dot{Q}_{F,p} + \dot{Q}_{F,n} \quad (3\text{-}27)$$

To determine the rate of the change of Joule heat, which is given by $\dot{Q}_J = -0.5I^2(R_p + R_n)$. For electrical resistance R_p, it can be achieved as:

$$R_p = \int_0^L \frac{\rho_p(x(T))}{A} dx(T) \quad (3\text{-}28)$$

We can further express the electrical resistance R_p as:

$$R_p = \int_0^L \frac{\rho_p(x(T))}{A} dx(T) = \int_{T_c}^{T_h} \frac{\rho_p(T)}{A} * \frac{k_p(T)}{Constant} dT = \frac{1}{B_1} \int_{T_c}^{T_h} \rho_p(T) * k_p(T) dT \quad (3\text{-}29)$$

Where $B_1 = A * Constant = \frac{A}{L} \int_{T_c}^{T_h} k_p(T) dT$. In the same way, we can get for n-type leg:

$$R_n = \frac{1}{B_2} \int_{T_c}^{T_h} \rho_n(T) * k_n(T) dT \quad (3\text{-}30)$$

Where $B_2 = \frac{A*\theta}{L} \int_{T_c}^{T_h} k_n(T) dT$.

Device performance can be written as:

$$\eta = \frac{output\ power}{Input\ heat\ power\ to\ the\ generator} \quad (3\text{-}31)$$

Apply (3-11) and (3-12) to the equation above, we can achieve:

$$\eta = \frac{P}{\dot{Q}_h} \quad (3\text{-}32)$$

$$\eta = \frac{I^2 R_L}{\dot{Q}_P + \dot{Q}_F + \dot{Q}_J} \quad (3\text{-}33)$$

We can maximize the device performance with respect to the external resistance R_L and the cross sectional area A.

$$\frac{\partial \eta}{\partial R_L} = 0 \quad (3\text{-}34)$$

$$\frac{\partial \eta}{\partial A} = 0 \quad (3\text{-}35)$$

Solving the two equations above, we can achieve that

$$\eta = \frac{\Delta T}{T_h} * \frac{\left(1 + \Delta T * \left(\frac{\bar{S}}{(\overline{\rho_n} * \overline{k_n})^{\frac{1}{2}} + (\overline{\rho_p} * \overline{k_p})^{\frac{1}{2}}}\right)^2 \left(\frac{S_h * T_h}{\bar{S} * \Delta T} - \frac{1}{2}\right)\right)^{\frac{1}{2}} - 1}{\frac{S_h * T_h}{\bar{S} * \Delta T}\left((1 + \Delta T * \left(\frac{\bar{S}}{(\overline{\rho_n} * \overline{k_n})^{\frac{1}{2}} + (\overline{\rho_p} * \overline{k_p})^{\frac{1}{2}}}\right)^2 (\frac{S_h * T_h}{\bar{S} * \Delta T} - \frac{1}{2}))^{\frac{1}{2}} + 1\right) - \frac{\Delta T}{T_h}} \quad (3\text{-}36)$$

Where $\Delta T = T_h - T_c$, $\bar{S} = \frac{1}{\Delta T} \int_{T_c}^{T_h} \left(S_p(T) - S_n(T)\right) dT$.

To optimize the efficiency, it can be shown that when $\theta = \left(\overline{k_p} * \overline{\rho_n} \middle/ \overline{k_n} * \overline{\rho_p}\right)^{1/2}$ and

$$R_L = \left(1 + \Delta T\left(\frac{\bar{S}}{(\overline{\rho_n} * \overline{k_n})^{\frac{1}{2}} + (\overline{\rho_p} * \overline{k_p})^{\frac{1}{2}}}\right)^2 (\frac{S_h * T_h}{\bar{S} * \Delta T} - \frac{1}{2})\right)^{1/2} (R_n + R_p)$$

Where $\overline{k_p} = \frac{1}{(T_h - T_c)} \int_{T_c}^{T_h} \left(k_p(T)\right) dT$, $\overline{\rho_p} = \frac{\int_{T_c}^{T_h} \rho_p(T) * k_p(T) dT}{\int_{T_c}^{T_h} k_p(T) dT}$;.

$$\overline{k_n} = \frac{1}{(T_h - T_c)} \int_{T_c}^{T_h} (k_n(T)) dT, \quad \overline{\rho_n} = \frac{\int_{T_c}^{T_h} \rho_n(T) * k_n(T) dT}{\int_{T_c}^{T_h} k_n(T) dT};$$

We can further simplify the expressions as:

$$\eta = \frac{\Delta T}{T_h} * \frac{\left(1 + \Delta T * m\left(\frac{S_h * T_h}{\overline{S} * \Delta T} - \frac{1}{2}\right)\right)^{\frac{1}{2}} - 1}{\frac{S_h * T_h}{\overline{S} * \Delta T}\left((1 + \Delta T * m(\frac{S_h * T_h}{\overline{S} * \Delta T} - \frac{1}{2}))^{\frac{1}{2}} + 1\right) - \frac{\Delta T}{T_h}} \quad (3\text{-}37)$$

If we set,

$$m = \left(\frac{\overline{S}}{(\overline{\rho_n} * \overline{k_n})^{\frac{1}{2}} + (\overline{\rho_p} * \overline{k_p})^{\frac{1}{2}}}\right)^2 \quad (3\text{-}38)$$

To validate the simulation derived above, we firstly applied our method to p-type $Hf_{0.3}Zr_{0.7}CoSn_{0.3}Sb_{0.7}$/nano-$ZrO_2$ (ZT~0.8) and n-type $Hf_{0.6}Zr_{0.4}NiSn_{0.995}Sb_{0.005}$ (ZT~1) data from Poon *et al.* in which they measured this p-n couple devices [37]. Results of the simulations in comparison with the measurement data for the HH module are shown in Figure 3-14. It can be seen that the simulation shows similar trend as the measurement data but slightly higher. This difference is due to the perfect contact assumption in our model, thus results in a higher efficiency.
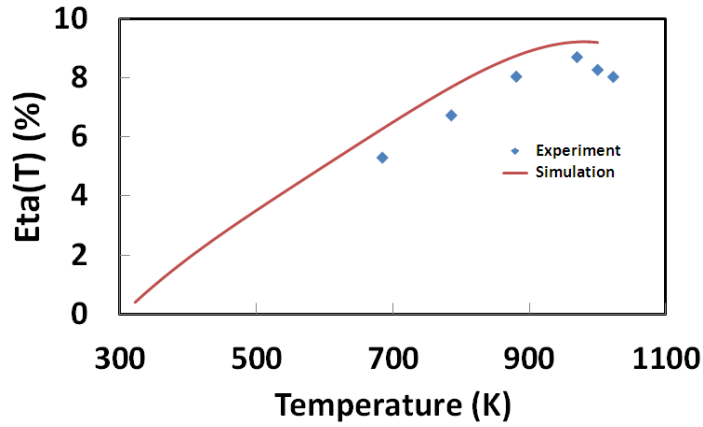
Figure 3-14. Heat-to-electric conversion efficiency for a single p-n couple made from p-type Hf$_{0.3}$Zr$_{0.7}$CoSn$_{0.3}$Sb$_{0.7}$/nano-ZrO$_2$ and n-type Hf$_{0.6}$Zr$_{0.4}$NiSn$_{0.995}$Sb$_{0.005}$ as a function of hot-side temperature.

We then applied our method on combination of the newly developed n-type Hf$_{0.65}$Zr$_{0.25}$Ti$_{0.15}$NiSn$_{0.995}$Sb$_{0.005}$/nano-ZrO$_2$ and recently reported p-type ZT~1.5 FeNb$_{0.88}$Hf$_{0.12}$Sb [65]. A power conversion efficiency 12.9% is achieved with hot side temperature of about 670 ^{o}C and cold side temperature of 40 ^{o}C as shown in Figure 3-15.
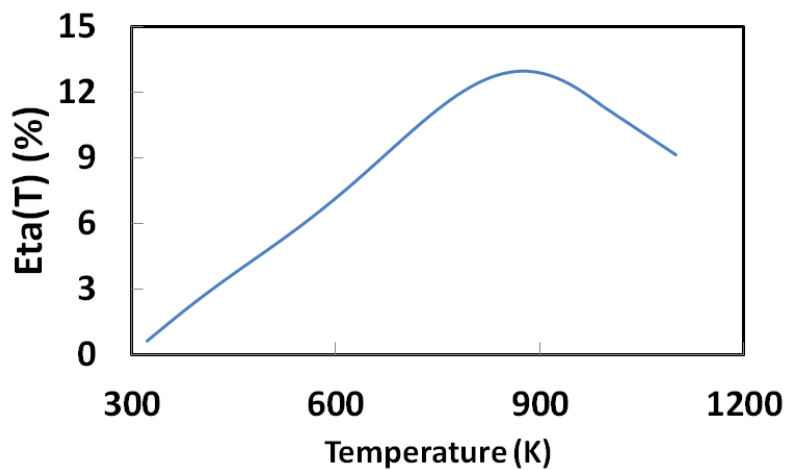
Figure 3-15. Heat-to-electric conversion efficiency for a single p-n couple made from p-type ZT~1.5 FeNb$_{0.88}$Hf$_{0.12}$Sb and n-type Hf$_{0.65}$Zr$_{0.25}$Ti$_{0.15}$NiSn$_{0.995}$Sb$_{0.005}$/nano-ZrO$_2$an as a function of hot-side temperature.

In summary, in this part a device efficiency model was built and applied to n-p couple from the newly developed n-type and recently reported p-type HH materials, reaching 12.9% power conversion efficiency for hot-side temperature of about 890K, indicating an important step towards wider application of HH materials for efficient power conversion devices.

3-4. Resonant states

3-4-1. Background

For semiconductor dopants, the normal dopants introduce extra impurity states in the band gap. When the introduced impurity states are close to conduction (valence) band edges, it is easier for the electrons (holes) be activated to the conduction (valence) band, and results in an increase of carrier concentration. In contrast, an exception to his mechanism exist: when the impurity states introduced by semiconductor dopants sit in the edge of conduction or valence band, the density of states in a narrow energy range will increase, forming resonant states which is shown in Figure 3-16.
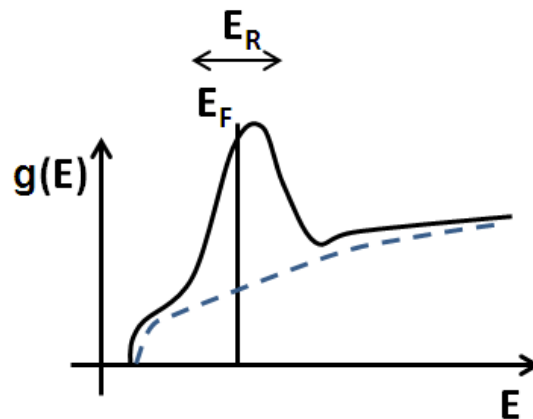
Figure 3-16. Localized resonant states in a narrow energy range E_R at Fermi level.

Mahan *et al.* made the prediction that the highest ZT for a given material can be achieved when the electronic density of states resembles a Dirac delta function at the Fermi level [65]. Since then, many systems have been studied to improve figure of merit through the formation of the resonant states at the Fermi level [51,66-68]. Heremans *et al.* [66] observed an increase ZT by a factor of 2 at 800 K by introducing 2% thallium to PbTe, and it was explained by the distortion in the density of states at the top of the valence band. First-principles density functional theory calculations were performed in both nitrogen-doped GaAs [67] and oxygen-doped ZnSe systems [68]. It was predicted that a localized sub-band in the density of states was created by the inclusion of impurities in both systems. For half-Heusler alloys, Simonson *et al.* [51] showed that small addition of vanadium substituted to the group IVB metal site of $Hf_{0.75}Zr_{0.25}NiSn$ increased the Seebeck coefficient of the compound at temperatures up to 650 K. They also showed experimental evidence for the presence of resonant states near the Fermi level in the alloys. With these results, it is important to investigate the role of resonant dopants on the thermoelectric properties of half-Heusler alloys with ZT > 1.

3-4-2. Experiments

Ingots of $(Hf_{0.6}Zr_{0.4})_{1-x}M_xNiSn_{0.995}Sb_{0.005}$ (M= V, Nb and Ta) with x= 0%, 0.2%, 0.5% and 1.0% were arc melted from appropriate quantities of elemental Hf, Zr, M, Sn and pre-melted $Sn_{90}Sb_{10}$ alloy under argon atmosphere. Then, these ingots were pulverized into 10 to 50 μm followed by consolidation using Spark Plasma Sintering technique. Samples were then first sintered at lower temperature of 1300 °C for 10 mins under 60 MPa to ensure single phase. Then, these samples

were annealed at a higher temperature of 1350 °C for another 20 mins under 60 MPa. The crystal structures of the samples were characterized by using x-ray diffraction on the PANalyticalX'Pert Pro MPD instrument. Energy-dispersive spectroscopy (EDS) was performed to check the distribution of the constituent elements of the compositions. Both the resistivity and thermopower were measured simultaneously using ZEM 3 system. The thermal conductivity was calculated from the sample density D, the specific heat C_p, and the thermal diffusivity α as $\kappa = DC_p\alpha$. The electrical thermal conductivity κ_e was estimated by using the Wiedenann-Franz relationship $\kappa_e = L\sigma T$, where L is the Lorenz Number which can be determined by using the equation proposed by Kim *et al.* [60] The lattice thermal conductivity κ_L was achieved by subtracting the electrical thermal conductivity κ_e from the total thermal conductivity κ.

The X-pattern of the most heavily V-doped sample $(Hf_{0.6}Zr_{0.4})_{0.99}V_{0.01}NiSn_{0.995}Sb_{0.005}$ is showed in Figure 3-17(a). Single HH structure was observed and no peaks of a second phase were detected. The compositional homogeneity checked by EDS line scanning shows a uniform distribution of V throughout the microstructure, which is similar to what reported earlier [51].
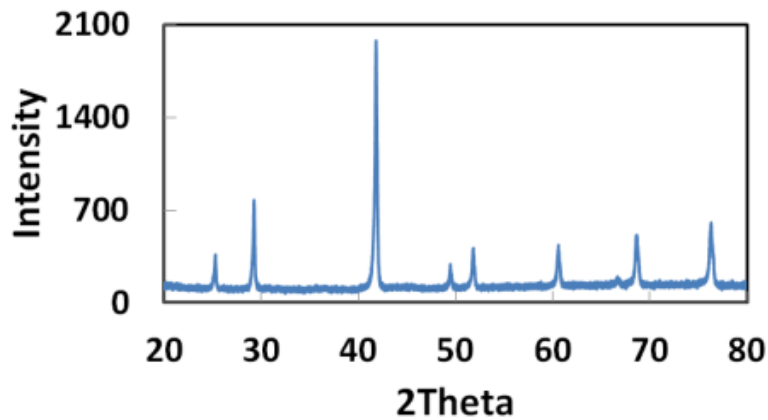
Figure 3-17. X-ray pattern for $(Hf_{0.6}Zr_{0.4})_{0.99}V_{0.01}NiSn_{0.995}Sb_{0.005}$.

The temperature dependences of the thermoelectric properties of the compositions are shown in Figure 3-18. It can be seen that as the doping level of V increases, the Seebeck coefficient rises over the entire temperature range 300K - 1000K accompanied by an increase in the resistivity. In the maximal case of 1% V-doped sample, the Seebeck coefficient increase by around 10% compared with no doping sample. Despite the increase in S, $PF = S^2/\rho$ of the sample remains similar compared with V-free sample due to the increase in ρ. In contrast, it is different when doping Nb or Ta.
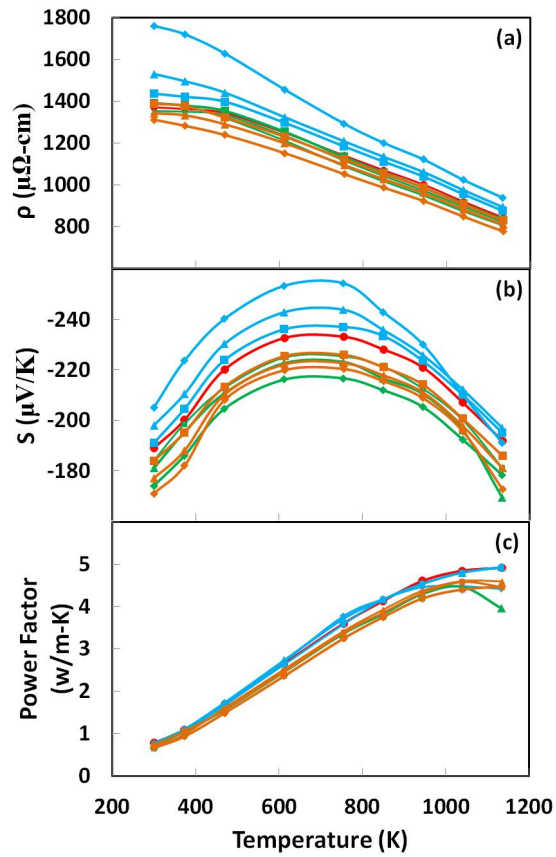
Figure 3-18. Thermoelectric properties of n-type $(Hf_{0.6}Zr_{0.4})_{1-x}M_xNiSn_{0.995}Sb_{0.005}$ (M = V, Nb and Ta), where x = 0 (red circle), x = 0.002 with M = V (blue square), x = 0.005 with M = V (blue triangle), x = 0.01 with M = V (blue rhombus), x = 0.002 with M = Nb (green square), x = 0.005 with M = Nb (green triangle), x = 0.01 with M = Nb (green rhombus), x = 0.002 with M = Ta (orange square), x = 0.005 with M = Ta (orange triangle), x = 0.001 with M = Ta (orange rhombus): (a) Electrical resistivity (ρ), (b) Seebeck coefficient (S), and (c) power factor.

3-4-3. Discussion

The doping effect difference between 3d V dopant and same group 4d Nb and 5d Ta dopants can be qualitatively understood in view of the hybridization of Group 5 dopant atoms and Hf(Zr) host atoms. Hybridization of the valence electrons between the Hf(Zr) and X (X=V, Nb, or Ta) atoms via their nearest-neighbor interaction υ causes bonding-antibonding splitting. The antibonding level lies above the Hf(Zr) atomic level E_{Hf} by an amount $\upsilon^2/|E_X-E_{Hf}|$, where E_X denotes the atomic level of X [69]. Since the atomic levels of Nb and Ta lie closer to the Hf level than that of V, the antibonding level that results from Hf-(Nb or Ta) hybridization is expected to lie somewhere further away from the conduction band edge. Moreover, based on the interatomic distance between Hf and X, the coupling matrix element υ would increase from V to Nb and Ta [70]. The weaker hybridization between V and Hf would also infer a more 'localized' nature of the V induced hybridized states near the conduction band edge, giving rise to the resonant states that decreases the electrical conductivity and enhances the thermopower.

The Hall coefficient $R_H = -1/nq$ reveals both the carrier type and carrier concentration, where n is the carrier concentration and q is the carrier charge. The carrier mobility μ_H can be deduced

from the relation ($\sigma = nq\mu_H$), where σ is the electrical conductivity. The effective band mass is calculated by assuming a single-band model [51]. Where $F_n(\eta_F)$ is the Fermi-Dirac integral, η_F is the reduced Fermi level defined as $\eta_F = E_F/k_BT$, k_B is the Boltzmann constant, m^* is the effective band mass. h is the Planck constant, and T is the temperature in K. The use of the single-band model for the above analysis was justified by previous study on the same system of materials [51]. The n, μ_H, and calculated m^* values are shown in Table I. It can be seen that n decreases for V doping and increases for Nb and Ta doping. The result further confirms the above-mentioned roles of the three dopants in the host alloy. The effective band mass for these alloys has been estimated to be larger than $2m_e$ [32,51]. The calculated m^* value increases from $2.16m_e$ for undoped sample to $2.72m_e$ for 1% V-doped sample, and slightly decreases for Nb and Ta-doped samples. This enhanced effective band mass might be attributed to a distortion in the density of states near the Fermi energy for V-doped samples [51].

The Hall coefficient was conducted on the samples to investigate the electronic transport properties. The carrier concentration and mobility values are shown in Table III.

Table III. Hall coefficient (R_H), carrier concentration (n), Hall mobility (μ_H) of $(Hf_{0.6}Zr_{0.4})_{1-x}M_xNiSn_{0.995}Sb_{0.005}$ (M= V, Nb and Ta) with x= 0%, 0.2%, 0.5% and 1.0%.

Condition	Hall coefficient R_H $(10^{-1}cm^3/C)$	Carrier concentration n $(10^{19}cm^{-3})$	Hall mobility μ_H $(cm^2/(V*s))$
$Hf_{0.6}Zr_{0.4}NiSn_{0.995}Sb_{0.005}$	-5.17	1.21	38.2
$(Hf_{0.6}Zr_{0.4})_{0.998}V_{0.002}NiSn_{0.995}Sb_{0.005}$	-5.31	1.18	37.5
$(Hf_{0.6}Zr_{0.4})_{0.995}V_{0.005}NiSn_{0.995}Sb_{0.005}$	-5.44	1.15	36.4
$(Hf_{0.6}Zr_{0.4})_{0.99}V_{0.01}NiSn_{0.995}Sb_{0.005}$	-5.79	1.08	33.8
$(Hf_{0.6}Zr_{0.4})_{0.998}Nb_{0.002}NiSn_{0.995}Sb_{0.005}$	-4.84	1.29	35.5

$(Hf_{0.6}Zr_{0.4})_{0.995}Nb_{0.005}NiSn_{0.995}Sb_{0.005}$	-4.88	1.31	36.4
$(Hf_{0.6}Zr_{0.4})_{0.99}Nb_{0.01}NiSn_{0.995}Sb_{0.005}$	-4.77	1.36	35.3
$(Hf_{0.6}Zr_{0.4})_{0.998}Ta_{0.002}NiSn_{0.995}Sb_{0.005}$	-4.71	1.32	36.1
$(Hf_{0.6}Zr_{0.4})_{0.995}Ta_{0.005}NiSn_{0.995}Sb_{0.005}$	-4.78	1.37	35.8
$(Hf_{0.6}Zr_{0.4})_{0.99}Ta_{0.01}NiSn_{0.995}Sb_{0.005}$	-4.69	1.46	36.1

To investigate the thermal conductivity of the compositions, the 1% doped samples were picked. The 1% doped sample shows the highest power factor compared with other doping levels. In addition, the higher amount of dopants helps reduce the lattice thermal conductivity due to the mass fluctuation effect. Thermal conductivity results are shown in Figure 3-19(a). The thermal conductivity is lower than the dopant-free sample as expected. The lattice thermal conductivity results are shown in Figure 3-19(b).
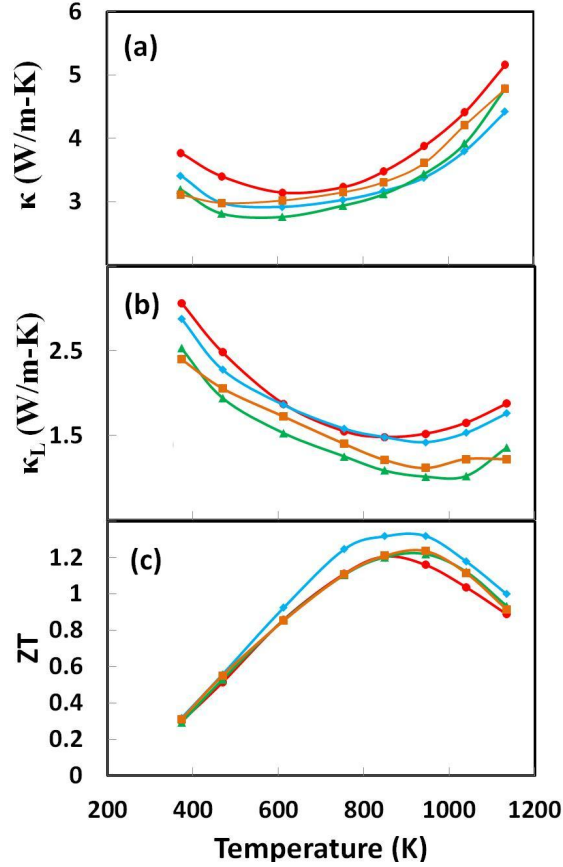
Figure 3-19. **(a) Thermal conductivity (κ), (b) lattice thermal conductivity (κ_L), and (c) ZT of n-type Hf$_{0.6}$Zr$_{0.4}$NiSn$_{0.995}$Sb$_{0.005}$ (red circle), and (Hf$_{0.6}$Zr$_{0.4}$)$_{0.99}$M$_{0.01}$NiSn$_{0.995}$Sb$_{0.005}$ (M = V, Nb and Ta), where M = V (blue rhombus), M = Nb (green triangle), M = Ta (orange square).**

Though the power factor of 1% V-doped sample is similar to that of the V-free sample, the figure of merit ZT increases due to the appreciable decrease of thermal conductivity, as shown in Figure 3-19(c). The maximum ZT value for (Hf$_{0.6}$Zr$_{0.4}$)$_{0.99}$V$_{0.01}$NiSn$_{0.995}$Sb$_{0.005}$ is about 1.31 at 850K. In contrast, the maximum ZT values of (Hf$_{0.6}$Zr$_{0.4}$)$_{0.99}$Nb$_{0.01}$NiSn$_{0.995}$Sb$_{0.005}$ and (Hf$_{0.6}$Zr$_{0.4}$)$_{0.99}$Ta$_{0.01}$NiSn$_{0.995}$Sb$_{0.005}$ are about 1.23.

3-4-4. Summary

A systematic investigation of the effect of vanadium, niobium, and tantalum dopants in n-type half-Heusler alloys based on $Hf_{0.6}Zr_{0.4}NiSn_{0.995}Sb_{0.005}$ is reported. The presence of V resonant states increases both electrical resistivity and Seebeck coefficient. In contrast, Nb and Ta act as normal dopants, as evident by the decrease in both resistivity and Seebeck coefficient. A maximum ZT of 1.3 at around 850K for n-type $(Hf_{0.6}Zr_{0.4})_{0.99}V_{0.01}NiSn_{0.995}Sb_{0.005}$ alloys is achieved without the need of nanostructures.

4. Lattice thermal conductivity calculation

Computationally efficient modeling of the thermal conductivity of materials is crucial for both experimental planning and theoretical understanding of thermal properties. To simulate the lattice thermal conductivity of materials and nanosystems, several approaches have been investigated in the literature, including: the Callaway model [73,74] which was derived from Boltzmann Transport Equation (BTE) [75-78], Monte Carlo simulations with varying phonon frequency dependence [79,80], and various methods to calculate the phonon mean free path (MFP) distributions, including analytical models, numerical results from molecular dynamics (MD) simulations [81], and first-principles calculations based on density functional theory [82]. Nan et al. [83,84] offered an effective medium approach to study two-phase heterogeneous systems. Later, Minnich and Chen utilized a modified EMA to predict the thermal conductivity of heterogeneous nanostructures [85]. This method modified the phonon mean free paths in both matrix materials and nanoparticles. The modification came from the assumption of phonon single particle scattering off the nanoparticles. However, this average T-matrix approximation (ATA) is only valid in small volume fractions since it is based on first-order T-matrix approximation [85]. Poon et al. introduced a differential effective medium (DEM) method, and extended the volume range from 0 to 1 [86,87]. The DEM approach incorporates multiple scattering that it is valid with high volume fractions.

In this chapter, a frequency-dependent differential effective medium model was developed. Effective scattering cross section which accounts for Rayleigh scattering, near geometrical scattering, and nanoparticle dispersion was incorporated. This method was performed on the prediction $ZrNi_2Sn/ZrNiSn$ nanocomposites and fully nanostructured half-Heusler ($Hf_{0.6}Zr_{0.4}NiSn_{0.99}Sb_{0.01}$ and $Hf_{0.5}Zr_{0.5}CoSn_{0.2}Sb_{0.8}$) systems. The model was further utilized to calculate lattice thermal conductivity of nanostructured solids. It accurately predicted the significant reduction in the thermal conductivity of Si and $Si_{80}Ge_{20}$ systems. The insight into the role of long wavelength phonons on the thermal conductivity of nanograined Si and Si80Ge20 alloys was achieved by using this model. This was further supported through the measurement with time-domain thermoreflectance.

4-1. Non-gray model of lattice thermal conductivity calculation

Previous studies showed that phonons with different frequencies will contribute differently in lattice thermal conductivity. It is important to have a frequency dependent model (non-gray model) to calculate lattice thermal conductivity. To derive the frequency dependent model, we start from Boltzmann equation:

$$\frac{\partial N_{q\lambda}}{\partial t} + \overrightarrow{v_{q\lambda}} \cdot \nabla N_{q\lambda} + \vec{F} \cdot \nabla_v N_{q\lambda} = (\frac{\partial N_{q\lambda}}{\partial t})_c \quad (4\text{-}1)$$

where $N_{q\lambda}$, $\overrightarrow{v_{q\lambda}}$, $\vec{F}$, and $(\frac{\partial N_{q\lambda}}{\partial t})_c$ are the phonon distribution function with vector $q=(q_i, q_j, q_k)$ in branch λ, phonon group velocity, external force and time rate of change of phonon distribution function according to collision, respectively.

According to relaxation approximation, the following expression is achieved:

$$(\frac{\partial N_{q\lambda}}{\partial t})_c = -\frac{N_{q\lambda} - N_{0q\lambda}}{\tau_q} \quad (4\text{-}2)$$

Where $N_{0q\lambda}$ is the equilibrium phonon distribution function, expressed as $N_{0q\lambda} = N_{q\lambda} - n_{q\lambda}$. n_q is the small deviation from local equilibrium distribution. When the system is in equilibrium state ($\frac{\partial N_{q\lambda}}{\partial t} = 0$) and in void of external force, the Boltzmann equation can be rewritten as:

$$\overrightarrow{v_{q\lambda}} \cdot \nabla N_{q\lambda} = -\frac{N_{q\lambda} - N_{0q\lambda}}{\tau_{q\lambda}} = -\frac{n_{q\lambda}}{\tau_{q\lambda}} \quad (4\text{-}3)$$

$$n_{q\lambda} = -\overrightarrow{v_{q\lambda}} \cdot \nabla T \frac{\partial n_{q\lambda}}{\partial T} \tau_{q\lambda} \quad (4\text{-}4)$$

Heat current in vector space can be expressed as: $\vec{J} = \sum_\lambda \iiint \hbar\omega_{q\lambda} n_{q\lambda} \overrightarrow{v_{q\lambda}} dq_i dq_j dq_k$. After applying equation above, the heat current can be further written as:

$$\vec{J} = -\sum_\lambda \iiint \hbar\omega_{q\lambda} (\overrightarrow{v_{q\lambda}} \cdot \nabla T \frac{\partial n_{q\lambda}}{\partial T} \tau_{q\lambda}) \overrightarrow{v_{q\lambda}} dq_i dq_j dq_k \quad (4\text{-}5)$$

Compare the equation above to with $\vec{J} = -\kappa \nabla T$, we can get:

$$\kappa_{ii} \frac{\partial T}{\partial i} + \kappa_{ij} \frac{\partial T}{\partial j} + \kappa_{ik} \frac{\partial T}{\partial k} = \sum_\lambda \iiint \hbar\omega_{q\lambda} \frac{\partial n_{q\lambda}}{\partial T} \tau_{q\lambda} (v_{q_i\lambda} v_{q_i\lambda} \frac{\partial T}{\partial i} + v_{q_i\lambda} v_{q_j\lambda} \frac{\partial T}{\partial j} +$$
$$v_{q_i\lambda} v_{q_k\lambda} \frac{\partial T}{\partial k}) dq_i dq_j dq_k \quad (4\text{-}6)$$

$$\kappa_{ji} \frac{\partial T}{\partial x} + \kappa_{jj} \frac{\partial T}{\partial y} + \kappa_{jk} \frac{\partial T}{\partial z} =$$
$$\sum_\lambda \iiint \hbar\omega_{q\lambda} \frac{\partial qp}{\partial T} \tau_{q\lambda} (v_{q_j\lambda} v_{q_i\lambda} \frac{\partial T}{\partial i} + v_{q_j\lambda} v_{q_j\lambda} \frac{\partial T}{\partial j} + v_{q_k\lambda} v_{q_k\lambda} \frac{\partial T}{\partial k}) dq_i dq_j dq_k \quad (4\text{-}7)$$

$$\kappa_{ki} \frac{\partial T}{\partial x} + \kappa_{kj} \frac{\partial T}{\partial y} + \kappa_{kk} \frac{\partial T}{\partial z} = \sum_\lambda \iiint \hbar\omega_{q\lambda} \frac{\partial n_{q\lambda}}{\partial T} \tau_{q\lambda} (v_{q_k\lambda} v_{q_i\lambda} \frac{\partial T}{\partial i} + v_{q_k\lambda} v_{q_j\lambda} \frac{\partial T}{\partial j} +$$
$$v_{q_k\lambda} v_{q_k\lambda} \frac{\partial T}{\partial k}) dq_i dq_j dq_k \quad (4\text{-}9)$$

Now we focus on κ_{ii} in volume V, the number of states between $q_i \sim q_i + dq_i$, $q_j \sim q_j + dq_j$ and $q_z \sim q_z + dq_z$ satisfies:

$$\int_0^{q_{mi}} g(q_i)dq_i = N \quad (4\text{-}10)$$

where $g(q_i)$ and q_{mi} are the density of states and the maximum wavevector in q_i direction. Then, we get $\kappa_{ii} = \sum_\lambda \int_0^{q_{mi}} \int_0^{q_{mj}} \int_0^{q_{mk}} \frac{V}{(2\pi)^3} \hbar\omega_{q\lambda} \frac{\partial n_{q\lambda}}{\partial T} \tau_{q\lambda}(v_{q_i})^2 dq_i dq_j dq_k$. Thermal conductivity can be written in terms of specific heat $(C(q))$, group velocity (v_q), and mean free path $(L_i(q))$ as:

$$\kappa_{ii} = \frac{1}{3} \int_0^{q_{mi}} \int_0^{q_{mj}} \int_0^{q_{mk}} C(q)v_q L_i(q) dq_i dq_i dq_i \quad (4\text{-}11)$$

Compare the equations above, the specific heat and mean free path can be expressed as:

$$C(q)_\lambda = \frac{V}{(2\pi)^3} \hbar\omega_{q\lambda} \frac{\partial n_{q\lambda}}{\partial T} = \frac{V}{(2\pi)^3} \frac{(\hbar\omega_{q\lambda})^2}{k_\beta T^2} \frac{e^{\frac{\hbar\omega_{q\lambda}}{k_\beta T}}}{(e^{\frac{\hbar\omega_{q\lambda}}{k_\beta T}} - 1)^2} \quad (4\text{-}12)$$

$$L_i(q)_\lambda = v_q * \tau_{q\lambda} \quad (4\text{-}13)$$

Based on Callaway's model, scattering mechanisms are reflected in relaxation time $\tau_{q\lambda}$:

$$\tau_\omega(q)^{-1} = A(\omega_{q\lambda})^4 + B(\omega_{q\lambda})^2 T^3 + v_s/l \quad (4\text{-}14)$$

Where the first term represents the scattering by point impurities, the second term is the umklapp process, the last term represents the boundary scattering, in which v_s is the sound velocity, l is the length characteristic of the material, which can be expressed as $(\rho * \sigma)^{-1}$, where ρ is the number of particles in a unit volume, and σ is cross section. The experimental specific heat C_{exp} is used to determine the unknown constant value associated with the density of state and the normalization factor in space. Assuming the temperature gradient ∇T is in x-direction, the thermal conductivity for a specific wavevector q can be expressed as:

$$\kappa(q) = \frac{D}{(2\pi)^3} 4\pi q^2 \sum_\lambda \hbar\omega_{q\lambda} \frac{\partial n_{q\lambda}}{\partial T} (v_{q\lambda})^2 \tau_{q\lambda} \quad (4\text{-}15)$$

To achieve the total thermal conductivity, we integrate $\kappa(q)$ in q space as:

$$\kappa = \int_0^{q_m} \kappa(q) dq \quad (4\text{-}16)$$

4-2. Effective scattering cross section

4-2-1. Scattering cross section

As we discussed previously, the length characteristic can be expressed as the density*scattering cross section. The Mie solution to Maxwell's equation shows that when phonon encounters particles the scattering mechanism changes from Rayleigh regime to geometric regime as the

phonon frequency increases [88-91]. In later work, Kim and Majumdar proposed a new pair of Rayleigh and geometric scattering cross sections as [92]:

$$\sigma_{\text{Rayleigh}} = \pi R^2 \chi^4 \left(\frac{\beta^2}{4} \left(\frac{\Delta M}{M} \right)^2 + 3\beta^8 \left(\frac{\Delta K}{K} \right)^2 \frac{(\sin\frac{\beta|\vec{q}|\delta}{2})^4}{\left(\frac{\beta|\vec{q}|\delta}{2} \right)^4} \right) \frac{\pi(\cos(4\chi)-1+(4\chi)\sin(4\chi)+32\chi^4-8\chi^2)}{16\chi^6} \quad (4\text{-}17)$$

$$\sigma_{\text{near geometrical}} = 2\pi R^2 (1 - \frac{\sin\left(2\chi\left(\frac{q'}{q}-1 \right) \right)}{\chi\left(\frac{q'}{q}-1 \right)} + \frac{(\sin\left(\chi\left(\frac{q'}{q}-1 \right) \right))^2}{(\chi\left(\frac{q'}{q}-1 \right))^2}) \quad (4\text{-}18)$$

Where $\vec{q}$, δ, and β are the scattering wave vector, the distance between the nearest atoms, and the trigonometric ratio, which is set to be $(1/\sqrt{2})$. Size parameter is defined as $\chi = qR$, where R is the radius of the spherical nanoparticle. The total scattering cross section is expressed as the combination of the two extreme regimes as the following:

$$\sigma_{total}^{-1} = \sigma_{\text{Rayleigh}}^{-1} + \sigma_{\text{near geometrical}}^{-1} \quad (4\text{-}19)$$

4-2-2. Grain size dispersion

In addition to cross section, experiments have shown that particle sizes ranges from nanometers to micrometers in most nanocomposites instead of being fixed at some constant value in models [93,94]. Theoretical work shows that the system contains a wide range of nanoparticle sizes will effectively scatter off phonons with different frequencies [11]. In simulation, a larger cross

section is achieved when a larger grain size standard is considered, thus the calculated lattice thermal conductivity will be lower.

In order to take the grain size distribution into consideration, the effective cross section can be written as the following [92]:

$$\sigma_{eff} = \int_{d_{min}}^{d_{max}} \sigma_{total}(x)F(x)dx \quad (4\text{-}20)$$

Where $F(x)$ is the normalized grain size distribution function. d_{max} and d_{min} are the lower and upper limit of grain size in system.

4-3. Effective medium theory

4-3-1. Average T-Matrix Approximation (ATA)

The effective medium theory is widely used to calculate the effective thermal conductivity of a heterogeneous system. The effective thermal conductivity κ^* can be expressed as:

$$\kappa^* = \kappa_0 + \frac{<T>}{I+<GT>} \quad (4\text{-}21)$$

Where κ_0 is the non-perturbation thermal conductivity. I is the unit matrix. G is the Green's function matrix. T is the transfer matrix, which can be expanded as $T = \sum_n T_n + \sum_{m \neq n} T_n G T_m + \sum_{m \neq n \neq l} T_n G T_m G T_l + \cdots$. Only the first order of T ($T = \sum_n T_n$) is kept to make the equation above soluble. The approximation is the independent particle approximation while multiple-particle interaction (higher order of T matrix) is ignored. $T_n = \frac{\delta \kappa_n \delta_n(r)}{(I - \delta \kappa_n \delta_n(r) G)}$. $\delta \kappa_n$ is the thermal conductivity perturbation from the embedding grain n. For a two-phase system, the effective thermal conductivity can be expressed as:

$$\kappa^* = \kappa_h \frac{(1+2\varphi)\kappa_p^* + 2(1-\varphi)\kappa_h}{(1-\varphi)\kappa_p^* + (2+\varphi)\kappa_h} \quad (4\text{-}22)$$

φ is the volume fraction of the second phase. κ_p^* is the effective thermal conductivity of the embedding particle system which can be written as:

$$\kappa_p^* = \frac{\kappa_p}{1 + \frac{\alpha \kappa_p}{\kappa_h}} \quad (4\text{-}23)$$

Where κ_p is the thermal conductivity of the embedding particle system, α is the thermal resistance parameter defined as $\alpha = R\kappa_h/(d/2)$. R and d are the thermal barrier resistance and the grain size of the embedded particle, respectively. Thus, the effective thermal conductivity of the two-phase system can be written as:

$$\kappa^* = \kappa_h \frac{\kappa_p(1+2\alpha) + 2\kappa_h + 2\varphi(\kappa_p(1-\alpha) - \kappa_h)}{\kappa_p(1+2\alpha) + 2\kappa_h - \varphi(\kappa_p(1-\alpha) - \kappa_h)} \quad (4\text{-}24)$$

4-3-2. Differential Effective Medium (DEM) approach

As we discussed above, ATA can only be applied to systems with low fractions of the second phase particles. To extend the calculation to the systems with higher volume fractions of the second phase, the Differential Effective Medium was discussed by Bruggeman [95]. Later, Poon *et al.* [86,87] reformulated it from a physical viewpoint and included higher-order terms (multi-particle scattering). Figure 4-1 shows the difference between the independent particles scattering in low volume fraction and multiple scattering in high volume fractions.
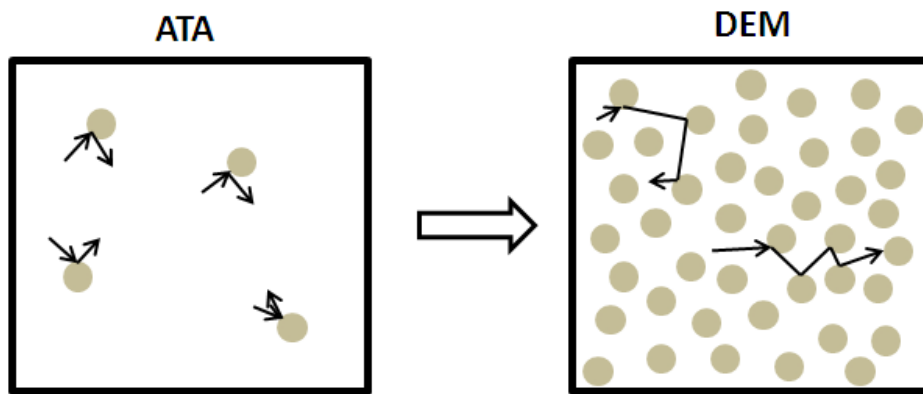

Figure 4-1 Independent particle scattering vs. multiple scattering.

The main idea behind DEM approach is shown in Figure 4-2. After adding $d\varphi$ of nanoparticles to the host, the thermal conductivity of the host $\kappa_h(\varphi)$ becomes $\kappa\left(\frac{\varphi}{1-d\varphi}\right)$. The updated thermal conductivity does not consider the phonon scattering from the added particles. $\kappa\left(\frac{\varphi}{1-d\varphi}\right)$ can be expanded as $\kappa(\varphi) + \varphi d\kappa(\varphi)$ when $d\varphi$ is small.
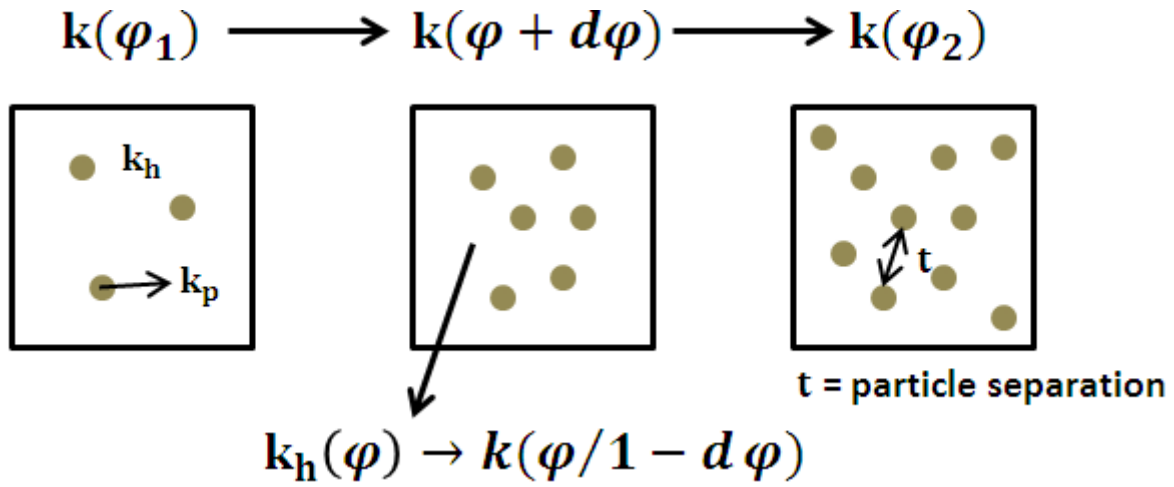
Figure 4-2 DEM approach: configuration of adding dφ of second phase in matrix.

Now we consider the phonon scattering from the added particles, the lattice thermal conductivity of the host for a specific wavevector can be expressed as:

$$\kappa_h(q, \varphi) = \frac{1}{3} C_h(q, \varphi) v_h(q, \varphi) L_{h,x}(q, \varphi) \quad (4\text{-}25)$$

The specific heat and velocity can be written as the following:

$$C_h(q, \varphi) = \varphi * C_{p,bulk}(q) + (1 - \varphi) * C_{h,bulk}(q) \quad (4\text{-}26)$$

$$\frac{1}{v_h(q,\varphi)} = \frac{\varphi}{v_{bulk,p}(q)} + \frac{1-\varphi}{v_{bulk,host}(q)} \quad (4\text{-}27)$$

The influence of the new added particles on phonon scattering can be reflected on mean free path as:

$$L_{h,x}(q, \varphi) = v_h(q, \varphi)(A(\omega_q)^4 + B(\omega_q)^2 T^3 + v\frac{6\varphi}{\pi a^3}(\sigma_{Rayleigh}^{-1} + \sigma_{near\ geometrical}^{-1})^{-1})^{-1}$$

(4-28)

Combining the equations above together, expand and only keep the first-order term, the lattice thermal conductivity of the host is updated as:

$$\kappa_h(q, \varphi) = \kappa(\varphi) + \varphi d\kappa(\varphi) - \frac{18\kappa(q,\varphi)^2(\sigma_{Rayleigh}^{-1} + \sigma_{near\ geometrical}^{-1})^{-1}}{\pi a^3 v(q,\varphi)C(q,\varphi)} d\varphi \quad (4\text{-}29)$$

After adding $d\varphi$ in the system, the overall thermal conductivity $\kappa(\varphi + d\varphi)$ can be written as:

$$\kappa(q, \varphi) = \kappa_{host}(q, \varphi)\left(1 + \frac{3d\varphi(\kappa_p(q)(1-\alpha(q,\varphi)) - \kappa_{host}(q,\varphi))}{\kappa_p(q)(1+2\alpha(q,\varphi)) + 2\kappa_{host}(q,\varphi) - d\varphi(\kappa_p(q)(1-\alpha(\varphi)) - \kappa_{host}(q,\varphi))}\right) \quad (4\text{-}30)$$

Since $d\varphi$ is small, we expand the equation above and only keep the first order. Then, $\kappa(q, \varphi + d\varphi)$ is given by:

$$\kappa(q, \varphi + d\varphi) = \kappa(q, \varphi) + \varphi d\kappa(q, \varphi) - \frac{18\kappa(q,\varphi)^2(\sigma_{Rayleigh}^{-1} + \sigma_{near\ geometrical}^{-1})^{-1}}{\pi a^3 C(q,\varphi)v(q,\varphi)} d\varphi \quad (4\text{-}31)$$

Since $\kappa(q, \varphi + d\varphi)$ can also be written as $\kappa(q, \varphi) + d\kappa(q, \varphi)$. After rearranging the equation above, the following differential form is observed:

$$d\kappa(q, \varphi) = \frac{3\kappa(q,\varphi)d\varphi}{(1-\varphi)} \left(\frac{\left(\kappa_p(q)(1-\alpha(q,\varphi))-\kappa(q,\varphi)\right)}{\left(\kappa_p(q)(1+2\alpha(q,\varphi))+2\kappa(q,\varphi)\right)} - \frac{6\kappa(q,\varphi)\left(\sigma_{Rayleigh}^{-1}+\sigma_{near\,geometrical}^{-1}\right)^{-1}}{\pi a^3 C(q,\varphi)v(q,\varphi)} \right) \quad (4\text{-}32)$$

The Rayleigh and near Geometrical cross sections are displayed in Chapter 4-1. To achieve the fully nanostructured system, let φ approach 1. When φ is equal to 1, there is no host, thus the term contains the cross section vanishes. Since there is no host when φ is approaching 1, this requires the numerator of the first term to be 0:

$$\kappa_p(q)\left(1 - \alpha(q, \varphi)\right) - \kappa(q, \varphi) = 0 \quad (4\text{-}33)$$

Now the thermal conductivity of the system becomes:

$$\kappa(q) = \frac{\kappa_p(q)}{1+\frac{\alpha_{p0}(q)*\kappa_p(q)}{\kappa_{p0}(q)}} \quad (4\text{-}34)$$

Where

$$\kappa_p(q) = \frac{1}{3}C_{bulk,p}(q)v_p(q)L_p(q) \quad (4\text{-}35)$$

$$\kappa_{p0}(q) = \frac{1}{3}C_{bulk,p}(q)v_p(q)L_{p0}(q) \quad (4\text{-}36)$$

$$L_p(q, \varphi) = v_p(q) \left(A(\omega_q)^4 + B(\omega_q)^2 T^3 + v_s/l \right)^{-1} \quad (4\text{-}37)$$

$$L_{p0}(q, \varphi) = v_p(q) \left(A(\omega_q)^4 + B(\omega_q)^2 T^3 \right)^{-1} \quad (4\text{-}38)$$

Based on the discussion above, DEM improves the thermal conductivity calculation compared with ATA, not only because it extends the volume fraction range from low volume fraction to 1, but also it incorporates multiple scattering.

4-4. Thermal conductivity calculation on half-Heusler alloys

4-4-1. Prediction on $ZrNi_2Sn/ZrNiSn$ (Full Heusler/Half-Heusler) nanocomposite

Frequency-dependent ATA calculation (discussed in Chapter 4-3-1) is performed on two systems: one is germanium (Ge) nanoparticles embedded in silicon (Si), and the other is the nano $ZrNi_2Sn$ full Heusler embedded in half-Heusler ZrNiSn system [96,97].
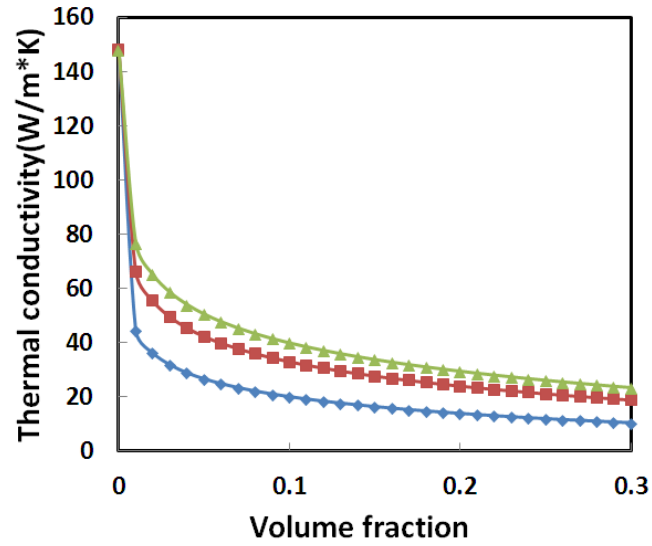
Figure 4-3. Lattice thermal conductivity vs. volume fraction φ in Ge/Si nanoparticle/matrix system at 300K. The grain sizes of Ge nanoparticles are set to be 10 nm (blue), 100 nm (red), and 200 nm (green).
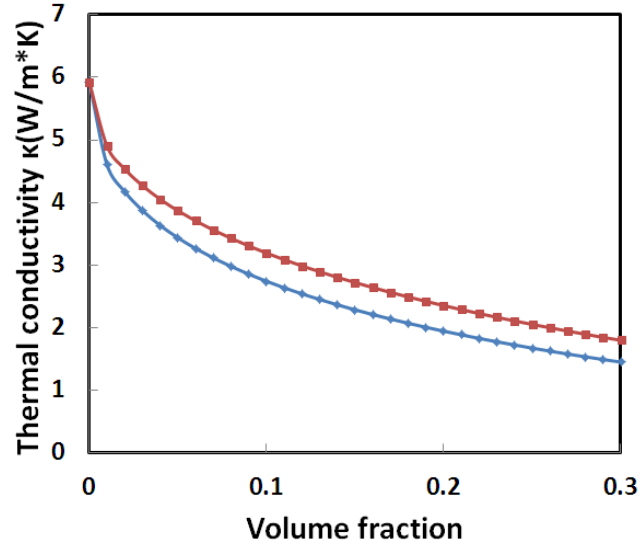

Figure 4-4. Lattice thermal conductivity vs. volume fraction φ in ZrNi$_2$Sn/ZrNiSn nanoparticle/matrix system at 300K. The grain sizes of ZrNi$_2$Sn nanoparticles are set to be 10 nm (blue) and 20 nm (red).

From Figure 4-3 and 4-4, it can be seen that as the volume fraction φ increases, the lattice thermal conductivity drops significantly. For a given volume fraction, the lattice thermal conductivity of system embedded with smaller nanoparticle sizes is lower. Since for the same volume fraction, a smaller particle size means higher interface density, thus leads to lower effective mean free path. It will result in reduced lattice thermal conductivity as expected. As we discussed above, ATA is derived when we consider the embedded particles as a small perturbation and ignore the effect from other embedded particles. This means that ATA is only valid when the volume fraction of the embedded particle is low.

4-4-2. Prediction on fully nanostructured $Hf_{0.6}Zr_{0.4}NiSn_{0.99}Sb_{0.01}$ and $Hf_{0.5}Zr_{0.5}CoSn_{0.2}Sb_{0.8}$ systems

Frequency-dependent DEM method (discussed in Chapter 4-3-2) is applied on $Hf_{0.6}Zr_{0.4}NiSn_{0.99}Sb_{0.01}$ and $Hf_{0.5}Zr_{0.5}CoSn_{0.2}Sb_{0.8}$ systems shown in Figure 4-5 and 4-6. It can be seen that as the grain sizes decreases, the lattice thermal conductivity drops significantly. When grain size changes from 500 nm to 5 nm, the lattice thermal conductivity deceases by almost 70%.
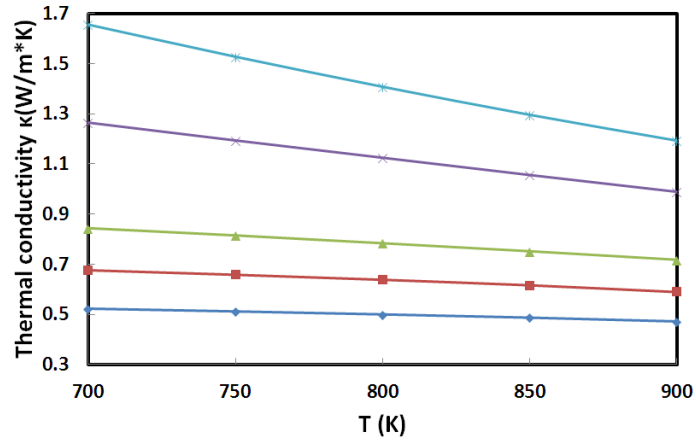
Figure 4-5. Lattice thermal conductivity vs. temperature in fully nanostructured $Hf_{0.6}Zr_{0.4}NiSn_{0.99}Sb_{0.01}$ system. The grain sizes are 5 nm (dark blue), 10 nm (red), 20 nm (green), 200 nm (purple), and 500 nm (light blue), respectively.
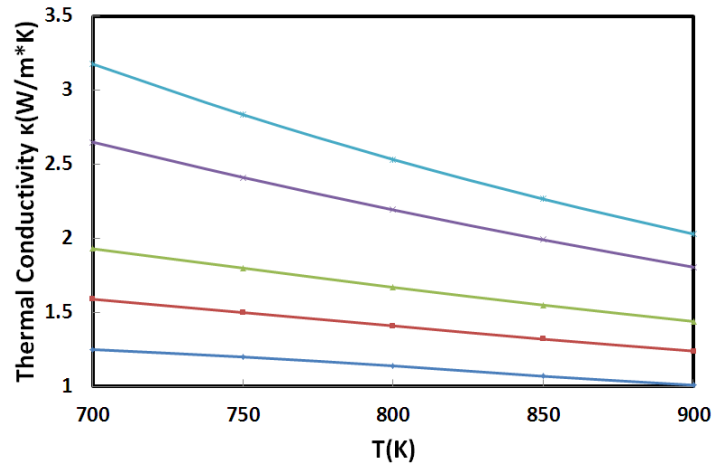
Figure 4-6. Lattice thermal conductivity vs. temperature in fully nanostructured $Hf_{0.5}Zr_{0.5}CoSn_{0.2}Sb_{0.8}$ system. The grain sizes are 5 nm (dark blue), 10 nm (red), 20 nm (green), 200 nm (purple), and 500 nm (light blue), respectively.

The simulation values show significant reduction in the lattice thermal conductivity in $Hf_{0.6}Zr_{0.4}NiSn_{0.99}Sb_{0.01}$ and $Hf_{0.5}Zr_{0.5}CoSn_{0.2}Sb_{0.8}$ systems. If the electronic power factor can be preserved in these materials, the figure of merit ZT will be greatly increased with the help of reduced lattice thermal conductivity.

4-5. Thermal conductivity accumulation in nanograined silicon and silicon-germanium alloys

We further apply the non-gray DEM method on the calculation of nanograined silicon and silicon-germanium alloys. The calculation results are then compared with the measurements of the frequency dependence in thermal conductivity with time domain thermoreflectance (TDTR). The silicon and silicon-germanium systems are picked since these systems are well studied in the TDTR community.

4-5-1. Non-gray DEM on silicon nanowires and Si/Ge nanocomposite

To validate the non-gray DEM method, we compare our calculation to measured thermal conductivity of silicon nanowires by Li *et al* [98]. Figure 4-7 shows the normalized thermal conductivity of silicon nanowires by using non-gray DEM and compare the calculation against various previous models. It can be seen that the non-gray DEM captures the thermal conductivity reduction in Si nanowires due to boundary scattering, which is similar to traditional phonon-transport models summarized by Yang and Dames [98].
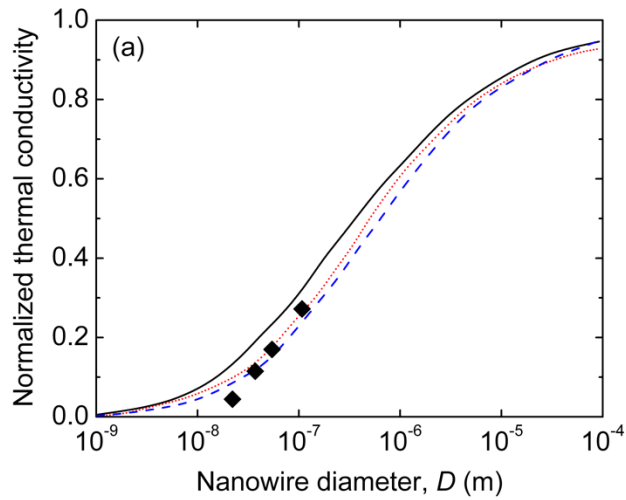
Figure 4-7. Normalized thermal conductivity of silicon nanowires calculated using the Holland model (solid, black) and BvKS model (dashed, blue), both of which were taken from Yang and Dames (ref [98]), as compared to our non-gray DEM (dotted, red), and the experimental data from Li *et al* (black diamonds).

We further calculate the lattice thermal conductivity of the Si/Ge nanocomposites. The Ge is in bulk matrix and the embedded particles have the diameter of 10 nm. The calculation results are shown in Figure 4-8. It can be seen from the figure that the non-gray DEM calculation shows more rapid reductions in the thermal conductivity as a function of volume fraction of Si at low volume fractions compared with other models (Minnich's gray and non-gray EMA models) [85]. In addition, the non-gray DEM simulation agrees well with Jeng's Monte Carlo (MC) simulations, which are also supported by experimental results. [99-101]
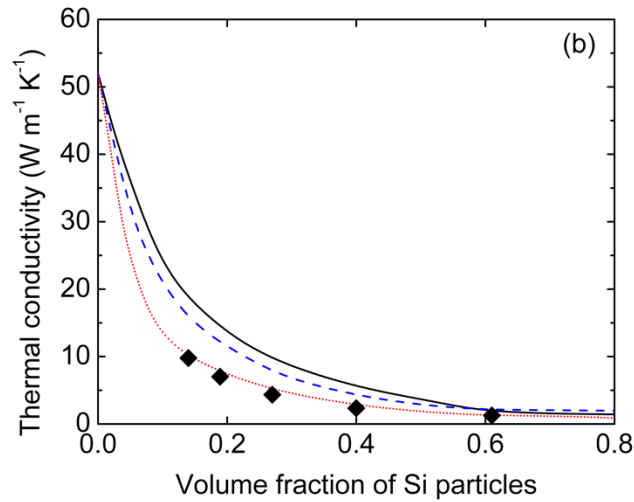
Figure 4-8. Lattice thermal conductivity κ_L of Si/Ge nanocomposite dependence on Si nanoparticles's volume fraction at room temperature (T=300K), with an average gran size $d = 10nm$. Non-gray DEM simulation with grain size dispersion-standard deviation of $0.577d$ (dotted, red) is compared with Jeng's MC simulation (black diamonds), gray EMA (black, solid), and non-gray EMA (blue dashed).

The have demonstrated the use of our modified DEM-based thermal conductivity model to predict the lattice thermal conductivity in both silicon nanowires and nanoparticle-in-matrix composites. Then, we extend the use of the method to fully nanograined Si and Si-Ge bulk systems to study accumulation effects on the thermal conductivity for these systems.

4-5-2. Sample synthesis

Si and $Si_{80}Ge_{20}$ were made into both bulk and nanostructured systems. For the bulk systems, ingots of Si and $Si_{80}Ge_{20}$ were prepared by using arc melting under an Argon atmosphere. The ingots were then pulverized into 1 to 30 μm size powders. These powders were then compacted

94

using SPS. Si and SiGe samples are sintered at 1280°C and 1210°C for 4 minutes under 60 MPa, respectively. To produce the nanostructured systems of Si and SiGe, the pulverized powders of Si and $Si_{80}Ge_{20}$ were loaded into the stainless steel vial, which is performed in a glove box under the protection of Argon atmosphere. Then the vial was loaded into a ball miller, and the powders were ball milled for 20 hours, 40 hours for both Si and $Si_{80}Ge_{20}$ systems. The powders then were consolidated by using SPS. The grain size of the SPSed disks was determined by using SEM on the cleaved cross section shown in Figure 4-9. For bulk Si and $Si_{80}Ge_{20}$ samples, the grain size ranges from $1 - 30$ μm, and 50-300 nm for the nanostructured systems.
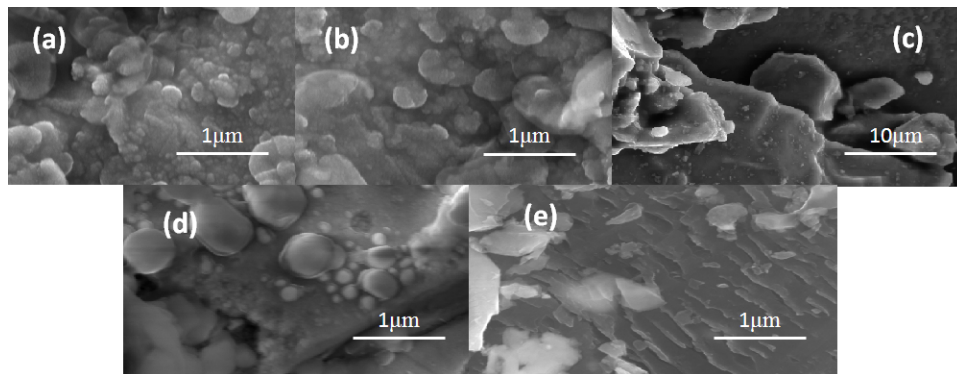

Figure 4-9. SEM micrographs for Si and $Si_{80}Ge_{20}$ systems: (a) Si 90 ± 28 nm , (b) Si 200 ± 37 nm, (c) $Si_{80}Ge_{20}$ 2 ± 0.17 μm, (d) $Si_{80}Ge_{20}$ 110 ± 21 nm, and (e) $Si_{80}Ge_{20}$ 73 ± 29 nm.

4-5-3. Thermal conductivity measurement via time domain thermoreflectance

We conducted measurements of the thermal conductivity of the Si and Si80Ge20 systems using TDTR with varying pump modulation frequencies. This approach has been vetted for accumulation effects study on the thermal conductivity for alloys. In this work, the consolidated

disks were mechanically polished to ensure mirror-like surfaces for TDTR measurement. The RMS roughness determined by mechanical profilometry maps was found to be 30 ± 10 nm. Sub--picosecond laser pulses emanating from a Ti:Sapph laser system at 80 MHz was used in this work, and the probe pulses were monitored via lock-in detection at the pump modulation frequency for up to of 5.5 ns using a mechanical delay stage. We then deposited a 80 nm thin film of Al on the surface of the sample acting as a thermal transducer, and fitted a thermal model to the decay to determine the thermal conductivity of both Si or $Si_{80}Ge_{20}$ samples. We assumed literature values for the other physical properties included in the thermal model including the heat capacity of Si, $Si_{80}Ge_{20}$, and Al [102,103]. We assume a reduced thermal conductivity of the Al film based on electrical resistivity measurements and the Wiedemann-Franz law, though we are insensitive to this parameter in our experiment due to our spot sizes and pump-probe delay. We also treat the thermal boundary conductance for the Al/Si or Al/$Si_{80}Ge_{20}$ interface as a free parameter in our model fit. The analysis methods are described in greater detail elsewhere [19,20,104]. Reported error in the thermal conductivity measurement arises from small thickness variation of the Al transducer and measurement of a number of different sites on the surface of each sample. Using laser spot sizes of 50 μm and 17 μm diameters for the pump and probe, respectively, allows us to assume nearly one dimensional heat transfer in the through-plane direction [20].

In order to probe various depths beneath the sample surface, we alter the modulation frequency of the pump beam ranging from 1.49 MHz to 12.2 MHz. We estimate depth probed during the TDTR measurements as the 2/e decay of the thermal gradient from the surface of the substrate, consistent with the recent findings of Koh *et al*. [105]. Thermal penetration depth is discussed in

Chapter 2. The use of our relatively large pump and probe spots sizes allow our TDTR measurements at the various frequencies to be directly related to the thermal transport physics in the cross plane direction, therefore reducing measurement sensitivities to in-plane non-diffusive thermal transport [22]. Furthermore, the use of Al as our thin film transducer will allow for direct comparison of our measurements to previous reports of Fourier failure in Si and Si-Ge-based systems without the potential for additional electron-phonon resistances in the metal film to complicate our results and analyses [106].

4-5-4. Cut-off mean free path determined by bridge function

The changing thermal penetration depth with the varying frequency during a TDTR experiments is related to the changes in the net heat flux [22,106-109]. Thus, the lattice thermal conductivity is separated into a high frequency mode component (diffusive) and a low frequency mode (quasi-ballistic). A plausible way to determine the cut-off mean free path is to equate the MFP to the thermal penetration depth in Eq. (2-3), and this MFP is used to determine the corresponding wavenumber q. This is usually called "hard cut".

There is also an alternative approach, "bridge function" [107]. In this model, the net heat-flux is written in the form of:

$$J = j^{LF} + j^{HF}$$

Where j^{LF} and j^{HF} are the low and high frequency mode contributions to the heat-flux. The equations for the low and high frequency mode heat fluxes for a given wavenumber q can be expressed as:

$$j(q)^{LF} = \frac{3}{5}(\text{MFP(q)})^2 \frac{\partial^2 j(q)^{LF}}{\partial x^2} - k(q)^{LF}\frac{\partial T}{\partial x}$$

$$j(q)^{HF} = -k(q)^{HF}\frac{\partial T}{\partial x}$$

After applying (4) and $\text{MFP(q)} = \tau_q v_q$, the following forms can be achieved:

$$j(q)^{LF} = \frac{3}{5}(\tau_q v_q)^2 \frac{\partial^2 j(q)^{LF}}{\partial x^2} - \left(\frac{D}{(2\pi)^3}4\pi q^2 \hbar\omega_{q\lambda}\frac{\partial n_{q\lambda}}{\partial T}\right)v_q^2 \tau_q \frac{\partial T}{\partial x}$$

$$j(q)^{HF} = -\left(\frac{D}{(2\pi)^3}4\pi q^2 \hbar\omega_{q\lambda}\frac{\partial n_{q\lambda}}{\partial T}\right)v_q^2 \tau_q \frac{\partial T}{\partial x}$$

The total heat-flux for both mode contributions can be achieved by integrating $j(q)^{LF}$ and $j(q)^{HF}$ over the q space. The cut-off wavenumber q can be obtained by varying q until the total heat-flux in the low frequency modes equals to the total heat-flux in the high frequency mode. The difference between using hard cut-off and the cut-off determined by using bridge function is shown in Figure 4-10.
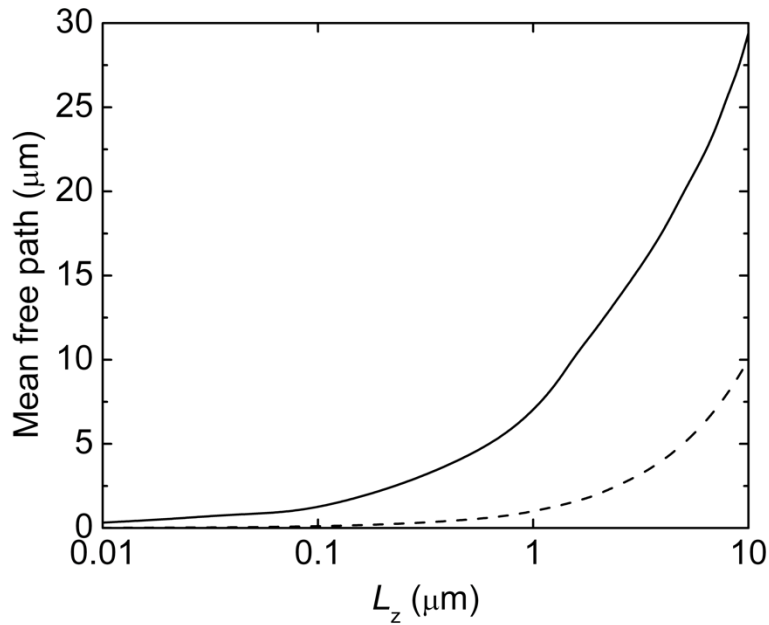
Figure 4-10. The cut-off mean free path vs thermal penetration depth for Si systems. The cut-off MFP determined by using bridge function (solid line) and the cut-off MFP determined by using hard cutoff (dashed line).

4-5-5 Discussion

Now we use this approach to analyze the TDTR data taken on the systems. The thermal conductivity values shown in figure 4-11 of the bulk and 200 nm average grain size silicon samples are measured to be 135 ± 20 W m^{-1} K^{-1} and 42 W $\pm$ 7 W m^{-1} K^{-1}, respectively. These values are in agreement with the thermal conductivity reported in a previous work for silicon with similar grain sizes [80].
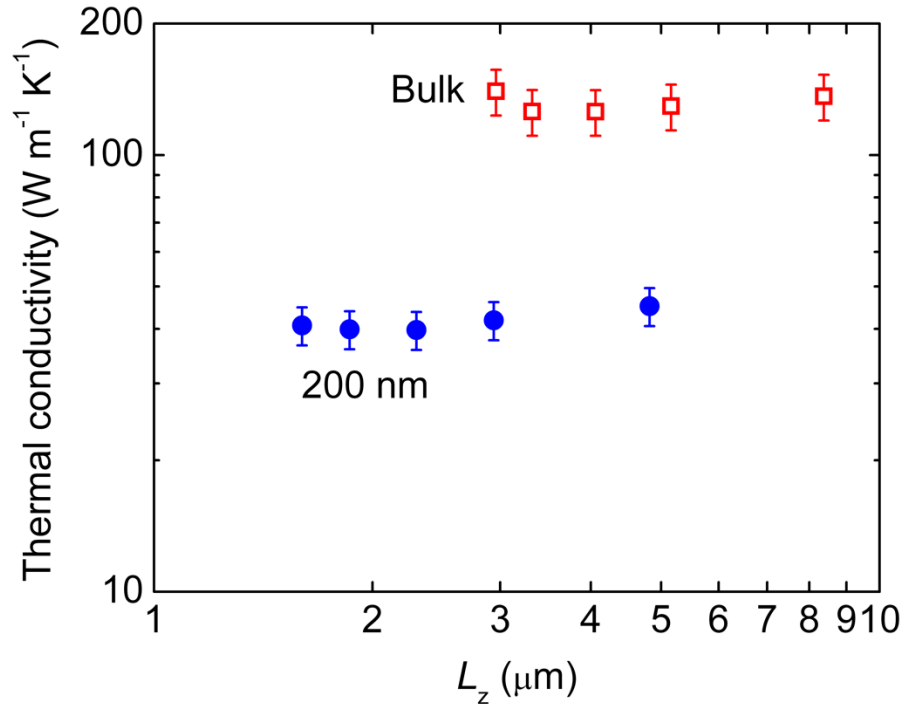
Figure 4-11. The accumulated thermal conductivity vs thermal penetration depth for bulk Si (blue rhombus), and Si samples with average grain size 200nm (red square).

Both the bulk and 200 nm-grained Si samples show a frequency independence in the measured thermal conductivity measured by TDTR.

A frequency dependence in the measured thermal conductivity is observed for the 90 nm-grained Si sample. This implies that as the measured thermal penetration depth increases, the thermal conductivity is also increased. This effect shows that the accumulation of the lattice thermal conductivity captures the heat carrying mean free paths in the system [22,105,106]. To understand it, three models are implemented: The first model is "Fixed Boundary Length" (FBL) model. In this model, the boundary scattering component in relaxation time uses a fixed length

scale, such as a film thickness or grain size. All the phonons with mean free paths greater than the fixed length scale will be scattered at the boundary and thus, they do not contribute to heat transport. Moving beyond the FBL, it is important to take the physical geometry of the structure into consideration. For example, circular boundaries and rectangular boundaries could impact phonon scattering differently. The boundary scattering can be considered as the length characteristic of the material l, which is discussed in section 4-1. The model calculation using the length characteristic is referred as the "Spectral Boundary Length" (SBL) model. The last model is the DEM model discussed in section 4-1. The figure 4-12 shows the accumulated thermal conductivity vs thermal penetration depth by using the three models discussed above. It can be seen that the geometry of the nanograins is not affecting the long mean free path phonons and scatters phonons in the middle of the Brillouin zone effectively as predicted by the SBL and DEM approaches, which account for scattering cross section instead of a simple and fixed boundary length scale. In addition, the use of bridge function and DEM approach yields a good agreement between the predicted trends and the measured frequency dependent thermal conductivity data.
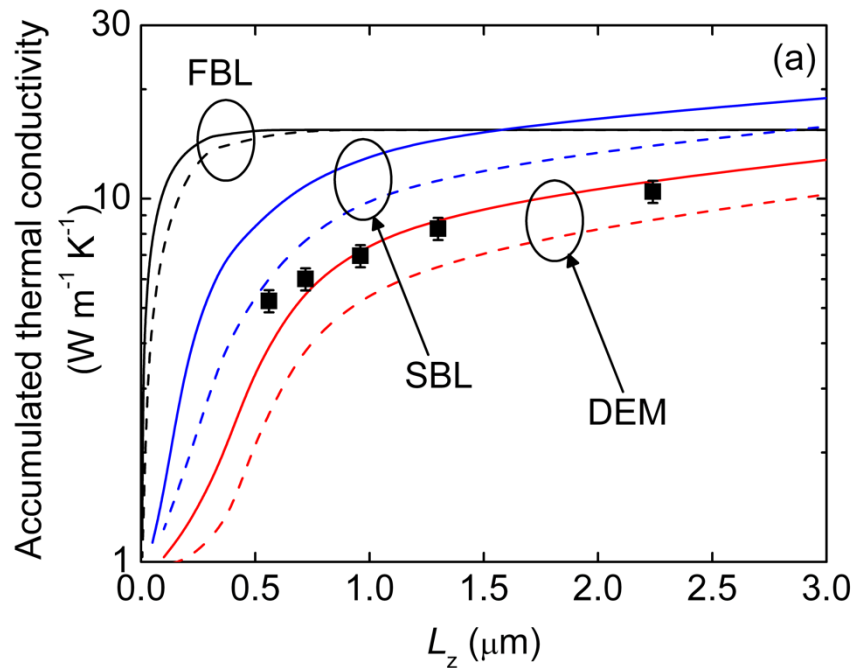
Figure 4-12. The accumulated thermal conductivity vs thermal penetration depth for Si samples with average grain size 90nm. The lines represent the modeled values. DEM with bridge function (red solid line) and DEM with hard cutoff (red dashed line), non-gray Callaway's method with bridge function (blue solid line), non-gray Callaway's method with hard cutoff (blue dashed line), gray Callaway's method with bridge function (green solid line), gray Callaway's method with hard cutoff (green dashed line).

In order to gain the quantitative insight into our experimental data, the spectral thermal conductivity for the 90 nm grained Si were performed via the FBL, SBL, and DEM approaches, shown in figure 4-13. Notably, phonons with wavelength larger than the grain sizes will not be scattered by the grain boundaries due to the properties of their characteristic lengths, while shorter wavelength phonons are limited by phonon-phonon scattering inside the grain. Both the SBL and DEM models capture this trend. The FBL model has a restriction in the propagation of

the phonon with long wavelength, as evident by the lack of contribution of long wave vector phonons to the spectral thermal conductivity.
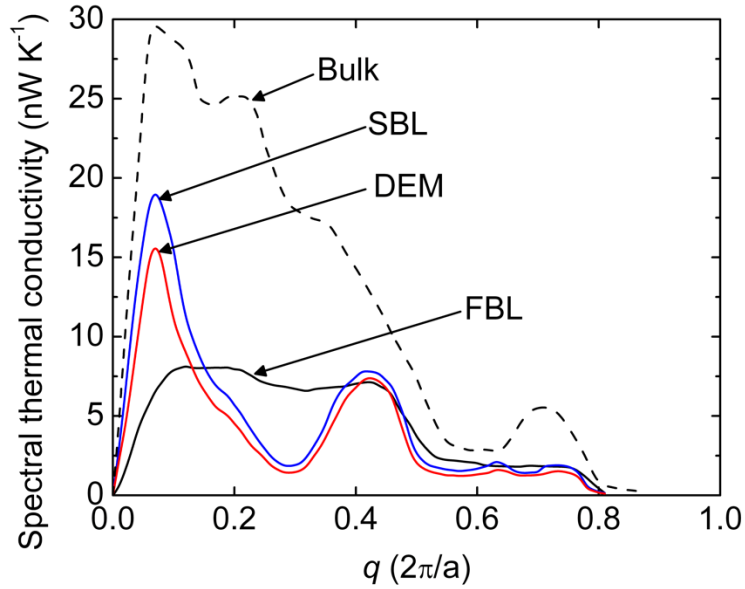

Figure 4-13. The spectral thermal conductivity vs wavevector for Si samples with average grain size 90nm. The lines represent the modeled values. DEM with bridge function (red solid line) and DEM with hard cutoff (red dashed line), non-gray Callaway's method with bridge function (blue solid line), non-gray Callaway's method with hard cutoff (blue dashed line), gray Callaway's method with bridge function (green solid line), gray Callaway's method with hard cutoff (green dashed line).

The simulation is further applied to nanograined $Si_{80}Ge_{20}$ systems with average grain size 2 μm, 110 nm, and 73 nm. Similar to what discussed in the nanograined Si system, we ascribe the frequency dependent TDTR data to phonons with mean free paths larger than the measurement volume (shown in figure 4-14).
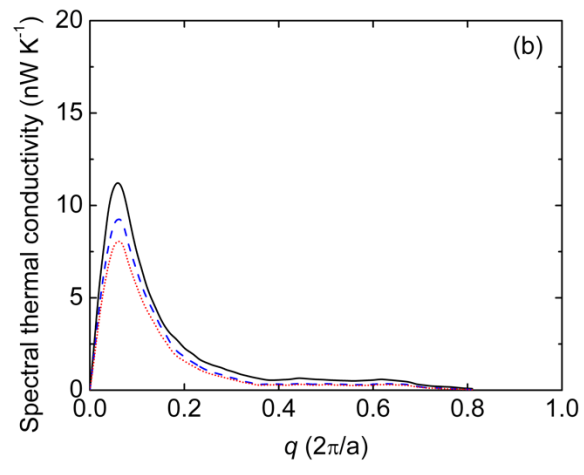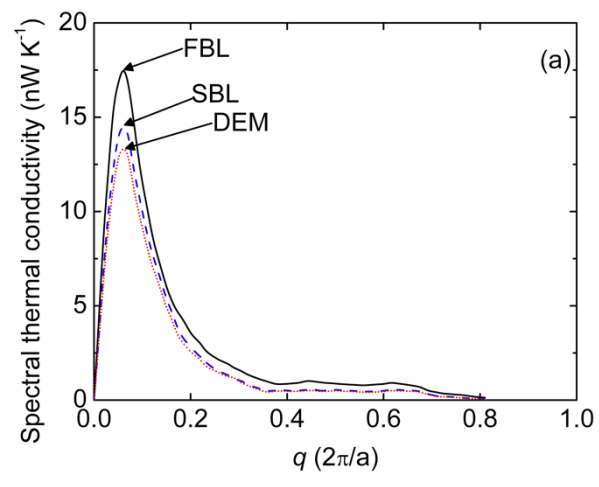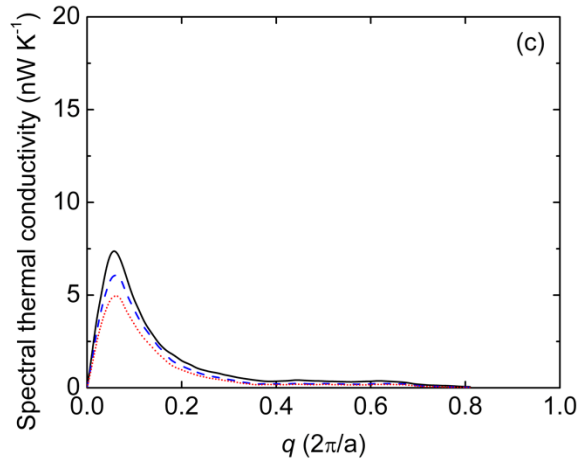
Figure 4-14. Spectral distribution of the thermal conductivity for $Si_{80}Ge_{20}$ samples with (a) average grain size 2μm, (b) 110nm, and (c) 73nm; DEM (red line), non-gray Callaway's method (blue line), gray Callaway's method (green line).

 The figure 4-15 shows the experimental data and the simulation results by using FBL, SBL, and DEM. These measured TDTR data show similar trends to previously reported frequency dependent data on SiGe alloys [22,105]. It can be seen that the DEM methods shows better agreement with the experimental data compared to the FBL and SBL models. In addition, the FBL model fails to account for the transport of phonons with long wavelength, since it assumes that theses phonons will scatter with the grain boundaries.
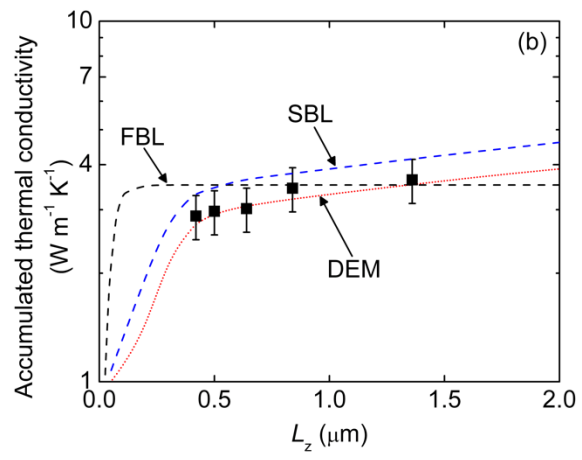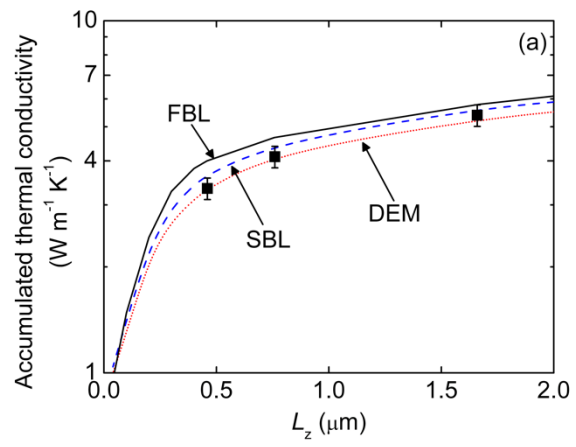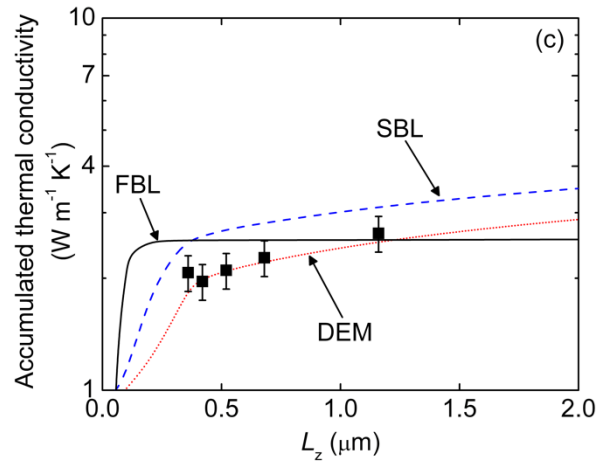
**Figure 4-15. Modeled (lines) and measured (points) accumulated thermal conductivity vs. thermal penetration depth for $Si_{80}Ge_{20}$ samples with (a) average grain size 2μm, (b) 110nm, and (3) 73nm.**

These results also suggest that it may not have as pronounced as an effect on lowering thermal conductivity by creating nanograins in crystalline alloys. It is predicted by traditional boundary scattering theories. The majority of the thermal transport in crystalline alloys is driven by the long wavelength. The scattering cross section of nanograins could be too small to create significant impact on the majority of the heat carrying phonons.

4-5-6 Conclusion

A frequency-dependent effective medium method is developed to calculate the lattice thermal conductivity of nanostructured Si and $Si_{80}Ge_{20}$ systems. The insight into the role of long wavelength phonons on the thermal conductivity of these systems is gained. Through thermal conductivity accumulation calculations, it can be shown that phonons with wavelengths larger than the average grain size will not be impacted by grain boundary scattering, counter to the

traditional notion that grain boundaries in solids will act as diffusive interfaces that will limit long wavelength phonon transport.

5. Acknowledgements

I would like to express my sincere appreciation to my advisor Dr. S. J. Poon for his constant guidance and financial support throughout these years, which are crucial for me to complete my study and research. I admire the help and guidance of Dr. P. E. Hopkins, and Dr. T. M. Tritt. I am also grateful to my dissertation committee, Dr. U. Chatterjee and Dr. J. Yoon.

I would like to express my gratitude to B. F. Donovan, A. Mehdizadeh and X. Zeng for their work in thermal conductivity measurement. I also wish to thank my colleagues, X. Li, A. S. Peterson, C. T. Ma, S. Gao, and X. Hu for their help and support through these years.

Finally, I would like to acknowledge with gratitude, the support and love of my parents, and my fiancé, Rena. They all provided encouragement to me and kept me going.

References

[1] C.Wood, *Rep. Prog. Phys.*, vol. 51, pp. 459–539, 1988.

[2] A. L. Rockwood, "Relationship of thermoelectricity to electronic entropy", *Physical Review A*, vol. 30, no. 5, pp. 2843–2844, 1984.

[3] S. R. De Groot, *Thermodynamics of Irreversible Processes*. Amsterdam: North Holland, 1951.

[4] N. W. Ashcroft and N. D. Mermin, *Solid State Physics*. Philadelphia: Saunders, 1976.

[5] E. Altenkirch, *Phys. Zeits.*, vol. 10, p. 560, 1909.

[6] E. ALtenkirch, *Phys. Zeits.*, vol. 12, p. 920, 1911.

[7] B. Poudel, Q. Hao, Y. Ma, Y. Lan, A. Minnich, B. Yu, X. Yan, D. Wang, A. Muto, D. Vashaee, X. Chen, J. Liu, M. S. Dresselhaus, G. Chen, and Z. Ren, "High-thermoelectric performance of nanostructured bismuth antimony telluride bulk alloys.," *Science (New York, N.Y.)*, vol. 320, no. 5876, pp. 634–8, May 2008.

[8] J. Androulakis, K. F. Hsu, R. Pcionek, H. Kong, C. Uher, J. J. D'Angelo, a. Downey, T. Hogan, and M. G. Kanatzidis, "Nanostructuring and High Thermoelectric Efficiency in p-Type Ag(Pb1 –ySny)mSbTe2 +m," *Advanced Materials*, vol. 18, no. 9, pp. 1170–1173, May 2006.

[9] J. P. Heremans, V. Jovovic, E. S. Toberer, A. Saramat, K. Kurosaki, A. Charoenphakdee, S. Yamanaka, and G. J. Snyder, "Enhancement of thermoelectric efficiency in PbTe by distortion of the electronic density of states.," *Science (New York, N.Y.)*, vol. 321, no. 5888, pp. 554–7, Jul. 2008.

[10] Y. Pei, H. Wang, and G. J. Snyder, "Band engineering of thermoelectric materials", *Advanced materials (Deerfield Beach, Fla.)*, vol. 24, no. 46, pp. 6125–35, Dec. 2012.

[11] K. Biswas, J. He, I. Blum, and C. Wu, "High-performance bulk thermoelectrics with all-scale hierarchical architectures," *Nature*, vol. 489, no. 7416, pp. 414–8, Sep. 2012.

[12] M. Rull-Bravo, A. Moure, J. F. Fernández, and M. Martín-González, "Skutterudites as thermoelectric materials: revisited", *RSC Adv.*, 2015, 5, 41653-41667.

[13] X. W. Wang, H. Lee, Y. C. Lan, G. H. Zhu, G. Joshi, D. Z. Wang, J. Yang, a. J. Muto, M. Y. Tang, J. Klatsky, S. Song, M. S. Dresselhaus, G. Chen, and Z. F. Ren, "Enhanced thermoelectric figure of merit in nanostructured n-type silicon germanium bulk alloy," *Applied Physics Letters*, vol. 93, no. 19, 193121, 2008.

[14] X. Yan, G. Joshi, W. Liu, Y. Lan, H. Wang, S. Lee, J. W. Simonson, S. J. Poon, T. M. Tritt, G. Chen, and Z. F. Ren, "Enhanced thermoelectric figure of merit of p-type half-Heuslers.," *Nano letters*, vol. 11, no. 2, pp. 556–60, Feb. 2011.

[15] G. Zeng, J. M. O. Zide, W. Kim, J. E. Bowers, A. C. Gossard, Z. Bian, Y. Zhang, A. Shakouri, S. L. Singer, and A. Majumdar, "Cross-plane Seebeck coefficient of ErAs:InGaAs∕InGaAlAs superlattices," *Journal of Applied Physics*, vol. 101, no. 3, 034502, 2007.

[16] K. Kishimoto, M. Tsukamoto, and T. Koyanagi, "Temperature dependence of the Seebeck coefficient and the potential barrier scattering of n-type PbTe films prepared on heated glass substrates by rf sputtering," *Journal of Applied Physics*, vol. 92, no. 9, 5331, 2002.

[17] D. M. Hulbert, A. Anders, D. V. Dudina, J. Andersson, D. Jiang, C. Unuvar, U. Anselmi-Tamburini, E. J. Lavernia, and A. K. Mukherjee, "The absence of plasma in 'spark plasma sintering'," *Journal of Applied Physics*, vol. 104, no. 3, 033305, 2008.

[18] "Molecular Biology," *Molecular Biology*, vol. 6, pp. 7–33, 1975.

[19] D. G. Cahill, "Analysis of heat flow in layered structures for time-domain thermoreflectance", *Review of Scientific Instruments*, 75 (12):5119-5122 (2004).

[20] P. E. Hopkins, J. R. Serrano, L. M. Phinney, S. P. Kearney, T. W. Grasser, and C. T. Harris. "Boundary scattering effects during electron thermalization in nanoporous gold", *Journal of Heat Transfer*, 132(8):081302–081302, 05 (2010).

[21] Aaron J. Schmidt, Xiaoyuan Chen, and Gang Chen, "Pulse accumulation, radial heat conduction, and anisotropic thermal conductivity in pump-probe transient thermoreflectance", *Review of Scientific Instruments*, 79(11):114902, (2008).

[22] R. B. Wilson, and D. G. Cahill, "Anisotropic failure of Fourier theory in time-domain thermoreflectance experiments", *Nature Communication*, 5:5075 (2014).

[23] C. Uher, J. Yang, S. Hu, D. T. Morelli, and G. P. Meisner, Phys. Rev. B **59**, 8615 (1999).

[24] Heinrich Hohl, Art P Ramirez, Claudia Goldmann, Gabriele Ernst, Bernd Wölfing, and Ernst Bucher, J. Phys.: Condens. Matter **11**, 1697 (1999).

[25] S. Bhattacharya, A. L. Pope, R. T. Littleton IV, T. M. Tritt, V. Ponnambalam, Y. Xia, and S. J. Poon, Appl. Phys. Lett. **77**, 2476 (2000).

[26] S. J. Poon, *Recent Trends in Thermoelectric Materials Research II*, Semiconduct. Semimet. **70**, 37 (2001). (Academic Press, New York, 2000).

[27] Do-young Jung, Ken Kurosaki, Chang-eun Kim, Hiroaki Muta, Shinsuke Yamanaka, J. Alloys Compounds **489**, 328 (2010).

[28] Killian Bartholome, Benjamin Balke, Daniel Zuckermann, Martin Koehne, Michael Mueller, Karina Tarantik, and Jan Koenig, J. Electr. Mater. **43**, 1775 (2014).

[29] Koji Miyamoto, Akio Kimura, Kazuaki Sakamoto, Mao Ye, Yitao Cui, Kenya Shimada, Hirofumi Namatame, Masaki Taniguchi, Shin-ichi Fujimori, Yuji Saitoh, Eiji Ikenaga, Keisuke Kobayashi, Junichi Tadano, and Takeshi Kanomata, Appl. Phys. Exp. **1**, 081901 (2008).

[30] Pengfei Qiu, Jiong Yang, Xiangyang Huang, Xihong Chen, and Lidong Chen, Appl. Phys. Lett. 96, 152105 (2010).

[31] Hanhui Xie, Heng Wang, Yanzhong Pei, Chenguang Fu, Xiaohua Liu, G. Jeffrey Snyder, Xinbing Zhao, and Tiejun Zhu, Adv. Func. Mater. 23, 5123 (2013).

[32] Hanhui Xie, Heng Wang, Chenguang Fu, Yintu Liu, G. Jeffrey Snyder, Xinbing Zhao and Tiejun Zhu, Scientific Report 4, 6888 (2014).

[33] Kimura Yoshisato and Y. W. Chai, JOM DOI: 10.1007/s11837-014-1233-3 (2014).

[34] Jan-Willem G. Bos, Downie and Ruth A. Downie, J. Phys.: Condens. Matter 26. 433201 (2014).

[35] Yaw Wang Chai, Kentaro Yoshioka, and Yoshisato Kimura, Scripta Mater. 83, 13 (2014).

[36] Cui Yu, Tie-Jun Zhu, Rui-Zhi Shi, Yun Zhang, Xin-Bing Zhao, and Jian He, Acta Mater. **57**, 2757 (2009).

[37] S. J. Poon, D. Wu, S. Zhu, W. J. Xie, T. M. Tritt, P. Thomas, and R, Venkatasubramanian, J. Mater. Res. **26**, 2795 (2011).

[38] Wenjie Xie, Anke Weidenkaff, Xinfeng Tang, Qingjie Zhang, Joseph Poon, and Terry M. Tritt, Nanomaterials **2**, 379 (2012).

[39] X. Yan, G. Joshi,W. Liu,Y. Lan, H. Wang, S. Lee, J. W. Simonson, S. J. Poon, T. M. Tritt, G. Chen, and Z. F. Ren, Nano Letters, **11**, 556 (2011).

[40] Xiao Yan, Weishu Liu, Hui Wang, Shuo Chen, Junichiro Shiomi, Keivan Esfarjani, Hengzhi Wang, Dezhi Wang, Gang Chen, and Zhifeng Ren, Energy Environ. Sci. **5**, 7543 (2012).

[41] Xiao Yan, Weishu Liu, Shuo Chen, Hui Wang, Qian Zhang, Gang Chen, and Zhifeng Ren, Adv. Energy Mater. **3**, 1195 (2013).

[42] Giri Joshi, Tulashi Dahal, Shuo Chen, Hengzhi Wang, Junichiro Shiomi, Gang Chen, Zhifeng Ren, Nano Energy **2**, 82 (2013).

[43] Giri Joshi, Ran He, Michael Engber, Georgy Samsonidze, Tej Pantha, Ekraj Dahal, Keshab Dahal, Jian Yang, Yucheng Lan, Boris Kozinsky, and Zhifeng Ren, Energy Environ. Sci. 7, 4070 (2014).

[44] Shuo Chen and Zhifeng Ren, Mater. Today, **16**, 387 (2013).

[45] Shuo Chen, Kevin C. Lukas, Weishu Liu, Cyril P. Opeil, Gang Chen, and Zhifeng Ren, Adv. Energy Mater. **3**, 1210 (2013).

[46] Huiyuan Geng and Hao Zhang, J. Appl. Phys. **116**, 033708 (2014).

[47] Beatriz Cordero, Verónica Gómez, Ana E. Platero-Prats, Marc Revés, Jorge Echeverría, Eduard Cremades, Flavia Barragán and Santiago Alvarez, Dalton Trans., DOI: 10.1039/b801115j (2008).

[48] N. N. Greenwood and A. Earnshaw, *Chemistry of the Elements (2nd ed.)* (Butterworth–Heinemann, Oxford and Woburn, 1997).

[49] S. R. Culp, S. J. Poon, N. Hickman, T. M. Tritt, and J. Blumm, Applied Physics Letters **88**, 042106 (2006).

[50] G.K. Williamson and W.H. Hall, X-ray line broadening from filed aluminium and wolfram. Acta Metallurgica **1.1** (1953): 22-31.

[51] J. W. Simonson, D. Wu, W. J. Xie, T. M Tritt and S. J. Poon, Phys. Rev. B **83**, 235211 (2011).

[52] M. Cutler and N. F. Mott, Phys. Rev. **181**, 1336 (1969).

[53] J. W. Simonson and S. J. Poon, J. Phys.: Condens. Matter **20**, 255220 (2008).

[54] H. Muta, T. Kanemitsu, K. Kurosaki, and S. Yamanaka, Mater.Trans. **47**, 1453 (2006).

[55] H. J. Goldsmid and J. W. Sharp, J. Electr. Mater. **28**, 7 (1999).

[56] S. Ogut and K. M. Rabe, Phys. Rev. B **51**, 10443 (1995).

[57] J. Callaway, "Model for Lattice Thermal Conductivity at Low Temperatures," *Physical Review*, vol. 113, no. 4, 1959.

[58] P. Klemens, "The thermal conductivity of dielectric solids at low temperatures (theoretical)," *Proceedings of the Royal Society A*, vol. 208, no. 1092, pp. 108–133, Aug. 1951.

[59] N. Mingo, D. Hauser, N.P. Kobayashi, M. Plissonnier, and A. Shakouri, "' Nanoparticle-in-Alloy ' Approach to Efficient Thermoelectrics : Silicides in SiGe," 2009.

[60]   H. S. Kim, Z. M. Gibbs, Y. Tang, H. Wang and G. J. Snyder, Appl. Phys. Lett. Mater., 3, 041506 (2015).

[61] V. I. Fistul, Heavily doped semiconductors, (Plenum, New York, 1969)

[62] M. Cutler and N. F. Mott, Phys. Rev., 181, 1336 (1969)

[63] B. Poudel, Q. Hao, Y. Ma, Y. Lan, A. Minnich, B. Yu, X. Yan, D. Wang, A. Muto, D. Vashaee, X. Chen, J. Liu, M. S. Dresselhaus, G. Chen and Z. Ren, Science, (2008) doi:10.1126/science.1156446

[64] H. J. Wu, L. -D. Zhao, F. S. Zheng, D. Wu, Y. L. Pei, X. Tong, M. G. Kanatzidis and J. Q. He, Nat Commun., 5, 4515 (2014)

[65] G. D. Mahan, and J. O. Sofo, *Proc. Natl. Acad. Sci.* **93**, 7436 (1996).

[66] J. P. Heremans, V. Jovovic, E. S. Toberer, A. Saramat, K. Kurasaki, A. Charoenphakdee, S. Yamanaka, and G. J. Snyder, *Science* **321**, 554 (2008).

[67] J. Wu, W. Shan, and W. Walukiewicz, *Semicond. Sci. Technol.* 17, 860 (2002).

[68] J.-H. Lee, J. Wu, and J. C. Grossman, *Phys. Rev. Lett.* **104**, 016602 (2010).

[69] H.P. Hjalmarson , P. Vogl, D.J.Wolford, and J.D.Dow, *Phys. Rev. Lett.* **44**, 810 (1980).

[70] C. Zhang, Z. Zhang, S. Wang, H. Li, J. Dong, N. Xing, Y. Guo, and W. Li, *J. Alloys and Compounds* **448**, 53 (2008).

[71] Y. I. Ravich, B. A. Efi mova, *I. A. Smirnov, Semiconducting Lead Chal-cogenides* (Plenum Press, New York, 1970).

[72] Y. I. Ravich, and L. Y. Morgovskii, *Sov. Phys. Semiconductors* **3**, 1278 (1970).

[73] J. Callaway, Phys. Rev. 113, 4 (1959).

[74] W. Kim, S. L. Singer, A. Majumdar, J. M. Zide, D. Klenov, A. C. Gossard and S. Stemmer, Nano Lett. 8, 7 (2008).

[75] R. G. Yang and G. Chen, Phys. Rev. B 69, 195316 (2004).

[76] C. Dames and G. Chen, J. Appl. Phys. 95, 2 (2004).

[77] R. G. Yang, G. Chen, M. Laroche, and Y. Taur, ASME J. Heat Transfer 127, 298–306 (2005).

[78] R. G. Yang, G. Chen and M. S. Dresselhaus, Phys. Rev. B 72, 125418 (2005).

[79] Q. Hao, G. Zhu, G. Joshi, Z. Wang, A. Minnich, Z. F. Ren, and G. Chen, Appl. Phys. Lett. 97, 063109 (2010).

[80] Z. Wang, J. E. Alaniz, W. Jang, J. E. Garay, and C. Dames, Nano. Lett. 11, 2206 (2011).

[81] G. Volz and Gang Chen, Appl. Phys. Lett. 75, 2056 (1999).

[82] P. Ravindran, Lars Fast, P. A. Korzhavyi, B. Johansson, J. Wills, and O. Eriksson, J. Appl. Phys. 84, 4891 (1998).

[83] C. W. Nan, "Effective medium theory of piezoelectric composites," *J.Appl.Phys.*, vol. 76, p. 1155, 1994.

[84] C. W. Nan, R. Birringer, D. R. Clarke, and H. Gleiter, "Effective thermal conductivity of particulate composites with interfacial thermal resistance," *Journal of Applied Physics*, vol. 81, no. 10, p. 6692, 1997.

[85] A. Minnich and G. Chen, "Modified effective medium formulation for the thermal conductivity of nanocomposites," *Applied Physics Letters*, vol. 91, no. 7, 073105, 2007.

[86] S. J. Poon and K. Limtragool, "Nanostructure model of thermal conductivity for high thermoelectric performance," *Journal of Applied Physics*, vol. 110, no. 11, 114306, 2011.

[87] S. Poon, A. Petersen, and D. Wu, "Thermal conductivity of core-shell nanocomposites for enhancing thermoelectric performance," *Applied Physics Letters*, vol. 102, no. 17, 173110, 2013.

[88] C. F. Bohren and D. R. Huffman, *Absorption and Scattering of Light by Small Particles*. New York: Wiley, 1998.

[89] H. C. van de Hulst, *Light Scattering by Small Particles*. New York: Dover, 1981.

[90] C. F. Ying and R. Truell, "Scattering of a Plane Longitudinal Wave by a Spherical Obstacle in an Isotropically Elastic Solid," *Journal of Applied Physics*, vol. 27, no. 9, p. 1086, 1956.

[91] N. G. Einspruch, E. J. Witterholt, and R. Truell, "Scattering of a Plane Transverse Wave by a Spherical Obstacle in an Elastic Medium," *Journal of Applied Physics*, vol. 31, no. 5, p. 806, 1960.

[92] W. Kim and A. Majumdar, J. Appl. Phys. 99, 084306 (2006).

[93] H. Li, X. Tang and Q. Zhang, *J. Electronic Materials*, vol. 38, no. 7, 2009.

[94] Y. Lan, A. J. Minnich, G. Chen, and Z. Ren, "Enhancement of Thermoelectric Figure-of-Merit by a Bulk Nanostructuring Approach," *Advanced Functional Materials*, vol. 20, no. 3, pp. 357–376, Feb. 2010.

[95] D. A. G. Bruggeman, "Berechnung verschiedener physikalischer Konstanten von heterogenen Substanzen. I. Dielektrizitätskonstanten und Leitfähigkeiten der Mischkörper aus isotropen Substanzen," *Ann. Phys.*, vol. 24, p. 636, 1935.

[96] H. Hohl, A.P. Ramirez, C. Goldmann, and G. Ernst, "Efficient dopants for ZrNiSn-based thermoelectric materials Efficient dopants for ZrNiSn-based thermoelectric materials," *J. Phys.: Condens. Matter*, vol. 11, p. 1697, 1999.

[97] W. Jeitschko, *Metall. Trans. A*, vol. 1, p. 3179, 1970.

[98] F. Yang and C. Dames, Physical Review B, 87:035437 (2013).

[99] M. S. Jeng, R. G. Yang, D. Song, and G. Chen, ASME J. Heat Transfer 130, 042410–1 (2008).

[100] H. Lee, MS thesis, MIT, Boston, MA (2005).

[101] M. S. Dresselhaus, G. Chen, Z. F. Ren, J. P. Fleurial, and P. Gogna, Second Annual Technical Report for NASA Contract No. NAS3-03108, (2005).

[102] C.Y. Ho, R.W. Powell, and P.E. Liley. Journal of Physical and Chemical Reference Data, 1(2):279–421, (1972).

[103] M.W. Chase. Jouranl of Physical and Chemical Reference Data, volume 1, National Institute of Standards and Technology, fourth edition, (1998).

[104] Aaron J. Schmidt, Xiaoyuan Chen, and Gang Chen. Review of Scientific Instruments, 79(11):114902, (2008).

[105] Y.K. Koh, D. G. Cahill, and B. Sun, Physical Review B, 90:205412 (2014).

[106]K. T. Regner, D. P. Sellan, Z. Su, C. H. Amon, A. J. H. McGaughey, and J. A. Malen. Broadband phonon mean freee path contributions to thermal conductivity measured using frequency domain ther- moreflectance. Nature Communications, 4:1640, (2013).

[107]A. T. Ramu and J. E. Bowers, Appl. Phys. Lett. 106 (26), 263102 (2015).

[108]K. T. Regner, L. C. Wei and J. A. Malen, Journal of Applied Physics, 118(23):235101 (2015).

[109]K. T. Regner, J. P. Freedman and J. A. Malen, Nanoscale and Microscale Thermophysical Engineering, 19(3):183-205, (2015).